

Subgrid modeling for reacting large eddy simulations

William H. Calhoon, Jr.

Georgia Inst. of Technology, Atlanta

Suresh Menon

Georgia Inst. of Technology, Atlanta

AIAA 34th Aerospace Sciences Meeting and Exhibit, Reno, NV Jan 15-18, 1996

Development of accurate combustion models is needed to aid in the design of improved combustors in both the aircraft and automotive industries. Numerical models capable of providing the necessary information must be able to predict the highly unsteady behavior associated with turbulent-chemistry interactions. One promising approach to investigate flows of practical interest is large-eddy simulation (LES). However, relatively few extensions to reacting flows have been made since additional closure problems arise from combustion-related terms which are difficult to model. One approach to combustion related subgrid closure is the linear-eddy mixing (LEM) model. This model separately treats the physical process of molecular diffusion and turbulent stirring so that an accurate picture of the interaction of the turbulence and the chemistry can be obtained. This paper investigates the LEM model for use in LES simulations of diffusion flames. (Author)

SUBGRID MODELING FOR REACTING LARGE EDDY SIMULATIONS

William H. Calhoun, Jr.* and Suresh Menon†
School of Aerospace Engineering
Georgia Institute of Technology
Atlanta, Georgia

ABSTRACT

Development of accurate combustion models is needed to aid in the design of improved combustors in both the aircraft and automotive industries. Numerical models capable of providing the necessary information must be able to predict the highly unsteady behavior associated with turbulent-chemistry interactions. One promising approach to investigate flows of practical interest is large-eddy simulation (LES). However, relatively few extensions to reacting flows have been made since additional closure problems arise from combustion related terms which are difficult to model. One approach to combustion related subgrid closure is the *linear-eddy mixing* (LEM) model. This model separately treats the physical process of molecular diffusion and turbulent stirring so that an accurate picture of the interaction of the turbulence and the chemistry can be obtained. This paper investigates the LEM model for use in LES simulations of diffusion flames.

1 INTRODUCTION

Accurate combustion models are needed for the design of improved combustors in both the aircraft and automotive industries. Designers seeking to improve combustor efficiency and reduce pollution emissions, for example, are increasingly limited by current modeling approaches. Turbulence plays a major role in these designs and must be treated carefully to yield accurate results. Numerical models for reacting flows capable of providing the necessary information must be able to predict the highly unsteady behavior associated with turbulent-chemistry interactions.

One approach for modeling turbulent reacting flows of practical interest is large-eddy simulation (LES). The underlying philosophy of LES is the explicit calculation of the large energy containing scales of motion which are directly affected by boundary conditions. These scales are difficult to model due their variability from one problem geometry to the next. The smaller scales of the flow are presumed to be more universal in nature and therefore more amenable to successful modeling. The LES equations of motion describe

the evolution of the large scales and are derived by applying a spatial filter function to the gas-phase Navier-Stokes reacting flow equations. This filtering process separates out the effects of the highly geometry dependent large scales from the more universal small scales. The filtering results in a set of equations describing the evolution of the large scale or resolved part of the flow variables. The effect of the small unresolved scales appears as additional subgrid terms in the resolved field equations. These subgrid terms must be modeled or additional equations for these terms derived in order to close the equation set.

Models for the subgrid-scale (SGS) terms in nonreacting, compressible flows have been developed (Erlebacher et al., 1990; Moin et al., 1991; Menon, 1991). However, relatively few extensions to reacting flows have been made. For this case, additional closure problems arise from combustion related terms which are difficult to model. These additional terms include: 1) the filtered reaction source terms, 2) the terms describing species transport due to turbulence, 3) the temperature-species correlations arising in the state equations.

LES of reacting flows has been previously applied to both premixed and nonpremixed combustion. For premixed fuels, Menon and Jou (1991) and Smith and Menon (1994) used the "G" equation to track the propagation of a thin flame front. The effect of chemical reactions on the propagation of the flame front was modeled phenomenologically in terms of a turbulent flame speed. This approach avoids the evaluation of filtered reaction source terms. The flow was also treated as a single component fluid with a heat source term which avoids the temperature-species correlations in the state equations. Menon *et al.* (1993a) have also investigated an innovative mixing model employing the "G" equation as a subgrid model in LES.

In the realm of nonpremixed combustion, Schumann (1989) and Sykes *et al.* (1992) applied LES to incompressible reacting atmospheric flows. For these simulations, the filtered chemical source terms were approximated in terms of the LES resolved field only and the effect of turbulent subgrid fluctuations was neglected. This type of assumption is valid for cases in which the chemistry is "slow" compared to the time scale for the decay of the species fluctuations. Fureby and Möller (1995) included first order subgrid mixing effects through an extension of the *eddy-dissipation* model of Magnussen and Hjertager (1976) to

*Graduate Research Assistant, Student Member AIAA.

†Associate Professor, Senior Member AIAA.

LES. Frankel *et al.* (1993) applied the assumed probability density function(pdf) method(Bilger, 1980) to LES of incompressible reacting flows with no heat release. A more general approach was proposed by Gao and O'Brien (1993) who advocated solving the pdf evolution equation(Pope, 1990) in the context of LES for incompressible flows.

Common in all these applications of LES to nonpremixed combustion is the use of the gradient diffusion assumption(Tennekes and Lumley, 1972) to model the species transport terms due to turbulence. Use of this type of assumption for reactive species is questionable(Dimotakis, 1989) and even dubious(Pope, 1979). An alternative subgrid modeling approach which avoids using this assumption has been proposed by Menon *et al.*(1993b) and McMurtry *et al.*(1992). They investigated the application of Kerstein's *linear-eddy mixing*(LEM) model(Kerstein, 1988, 1989, 1990, 1991 1992) as a subgrid model in LES of turbulent premixed and diffusion flames. These initial investigations demonstrated the good qualitative characteristics of this approach for simulations in which the chemistry was uncoupled from the fluid dynamics.

The LEM model used in these calculations separately treats the physical process of molecular diffusion and turbulent stirring at the small scales so that an accurate picture of the interaction of the turbulence and the chemistry can be obtained. The capabilities of the LEM model have been demonstrated for mixing in grid turbulence(Kerstein, 1988), reacting mixing layers (Kerstein, 1989), jet diffusion flames(Kerstein, 1990, 1992; Menon *et al.*, 1994; Calhoon *et al.*, 1995) and for premixed flames(Menon and Kerstein, 1992). The advantages of this mixing model over other formulations make it an excellent candidate as a subgrid mixing model for use in LES.

This paper describes the application of Kerstein's LEM model for use in LES simulations of diffusion flames. This approach may be applied to the general case of compressible flows with high heat release reactions. In this study, however, the capabilities of the method to model mixing and reaction of diluted fuels with low heat release reactions is evaluated. The case of high heat release will be investigated in a future study.

The following sections of this paper discuss the LES equations of motion for reacting flows and describe the subgrid closure modeling. A brief description of the basic LEM model is given and its application as a subgrid model is presented. The numerical method used in the calculations is also described. Results of the method applied to turbulent reacting mixing layers are presented and discussed.

2 LES SIMULATION MODEL

The LES reacting flow equations are derived by the convolution of a spatial filter function with the Navier-Stokes equations describing mass, momentum, energy and species conservation for a multi-component fluid. The filtering results in a set of equations for the large scale or resolved part of the flow variables. The resolved part of any vari-

able M which varies in space x_j and time t is defined by the convolution,

$$\overline{M}(x_j, t) = \int_{\Xi} M(z_j, t) G(x_j - z_j) dz_j \quad (1)$$

where G is the spatial function which has a characteristic width Δ_{LES} . In this study, the *box* filter is used so that Δ_{LES} is equal to the computation grid cell width. For compressible flows, it is customary to introduce mass weighted or Favre filtering(Erlebacher *et al.*, 1990) and express the resolved field as $\overline{M} = \overline{\rho M} / \overline{\rho}$. The turbulent field variable M can now be decomposed into the resolved and unresolved parts as $M = \overline{M} + M''$, where M'' is the unresolved or fluctuating subgrid component.

Applying the filtering defined in equation (1) to the governing equations results in the LES equations of motion for reacting flows. These equations describe the temporal and spatial evolution of the resolved variables $\{\overline{\rho}, \overline{\rho u_j}, \overline{\rho E}, \overline{\rho Y_k}\}$ where ρ , u_j , E and Y_k are the density, j th component of velocity, specific total energy and k th species mass fraction respectively. These equations are given in Fureby and Möller(1995) and are not repeated here for brevity.

The effect of the small unresolved scales appears as additional unknown terms in the resolved field equations. In the momentum equation, two additional terms arise which are the SGS stress tensor τ_{ij}^{sgs} and the filtered viscous stress tensor $\tilde{\tau}_{ij}$. The unclosed terms in the filtered energy equation are the SGS total enthalpy flux H_j^{sgs} , the filtered heat flux \tilde{q}_j and the SGS viscous work term σ_j^{sgs} . Other subgrid terms representing convective species fluxes $\Phi_{k,j}^{sgs}$, species diffusive fluxes $\theta_{k,j}^{sgs}$ and the filtered species production rate \tilde{w}_k also appear in the species conservation equations. See Fureby and Möller(1995) for a description of these terms.

In addition to the conservation equations, the equation of state for a multi-component fluid must also be filtered. The unfiltered state equation is given by $p = \rho R^\circ T \sum_{k=1}^K Y_k / W_k$ where T is the temperature, K is the total number of species, R° is the universal gas constant and W_k is the k th species molecular weight. Applying the filtering to this equation results in,

$$\overline{p} = \overline{\rho} R^\circ \tilde{T} \sum_{k=1}^K \frac{\tilde{Y}_k}{W_k} + \overline{\rho} R^\circ \sum_{k=1}^K \frac{T_k^{sgs}}{W_k} \quad (2)$$

where T_k^{sgs} contains temperature-species correlations and is given by $T_k^{sgs} = \overline{\tilde{Y}_k T} - \tilde{Y}_k \tilde{T}$.

The filtering must also be applied to the caloric equation of state $e = h - p/\rho$ with the mixture enthalpy h specified in terms of the species heat of formation and specific heats $c_{p,k}$ (Williams, 1985). Specifying the $c_{p,k}$'s in terms of polynomial approximations(Kee *et al.*, 1989), higher order temperature-species correlations appear in the filtered caloric equation of state which are of the form,

$$T_k^{sgs, n} = \sum_{k=1}^K \sum_{n=2}^N a_{k,n} \frac{(\overline{\tilde{Y}_k T^n} - \tilde{Y}_k \tilde{T}^n)}{n} \quad (3)$$

where $a_{k,n}$ is the n th coefficient of the N th order polynomial approximating $c_{p,k}$.

In order to solve the LES conservation equations, all these additional terms must be closed with appropriate subgrid models. The SGS stress tensor τ_{ij}^{sgs} and the enthalpy flux term H_j^{sgs} are not unique to reacting flows but also appear in the compressible nonreacting LES equations. As a result, standard models for these terms may be adopted. In this study, τ_{ij}^{sgs} and H_j^{sgs} are modeled using the compressible extension (Nelson, 1995) of the *Localized Dynamic k-Equation Subgrid-Scale* (LDKSGS) model of Kim and Menon (1995). This model requires the solution of an additional modeled equation for the subgrid turbulent kinetic energy defined as $k^{sgs} = (\overline{u_i u_i} - \tilde{u}_i \tilde{u}_i)/2$. The subgrid terms related to diffusive processes (i.e. $\theta_{k,j}^{sgs}$, σ_j^{sgs} and the unresolved parts of $\tilde{\tau}_{ij}$ and \tilde{q}_j) are generally neglected in both reacting and nonreacting simulations. This is true even for high temperature flames where molecular properties may change rapidly (e.g. Fureby and Möller, 1995). This approach is adopted for the present study of low heat release flames.

The principle difficulty in reacting LES simulations is the proper modeling of the combustion related terms involving the temperature and species which are: 1) the convective species fluxes $\Phi_{k,j}^{sgs} = \bar{\rho}(\tilde{Y}_k \tilde{u}_j - \tilde{Y}_k \tilde{u}_j)$ due to turbulent fluctuations, 2) the temperature-species correlations T_k^{sgs} and $T_k^{sgs,n}$ and 3) the filtered species mass production rate \bar{w}_k .

The transport term $\Phi_{k,j}^{sgs}$ is almost universally modeled in LES using the gradient diffusion assumption. $\Phi_{k,j}^{sgs}$ may then be approximated by an eddy viscosity type model (Tennekes and Lumley, 1972) of the form $\Phi_{k,j}^{sgs} = -\bar{\rho}(\nu_T/Sc_t)\partial\tilde{Y}_k/\partial x_j$, where Sc_t is the turbulent Schmidt number and ν_T is the eddy viscosity expressed in terms of k^{sgs} . Application of the eddy viscosity type model has been reasonably successful for approximating τ_{ij}^{sgs} and H_j^{sgs} . However it has been less successful when used for species transport. Frankel *et al.* (1993) attributed use of this assumption as the source of errors in comparison of reacting LES simulations with direct numerical simulation (DNS) data. Also, the magnitude of the modeled $\Phi_{k,j}^{sgs}$ may overwhelm the physical molecular diffusion terms causing the final solution to be invariant with the diffusion process. This is a serious problem because molecular diffusion is known to be a controlling phenomena in combustion processes even at high Reynolds numbers (Re) (Broadwell and Mungal, 1991).

Subgrid modeling for the temperature-species correlations T_k^{sgs} and $T_k^{sgs,n}$ appearing in the state equations has received little or no attention. For low heat release these correlations can be expected to be negligible. For simulations with high heat release this is not expected to be true. For example, Calhoun and Menon (1995) found T_k^{sgs} to be significant in an H_2 - air turbulent jet simulated using the LEM model. However, due to the difficulty and uncertainty in modeling these terms they are generally neglected (e.g. Fureby, 1995) with little justification. Alter-

natively, an evolution equation for T_k^{sgs} can be derived but the third order terms appearing in this equation are even more difficult to model.

The final term requiring modeling is the filtered species mass production rate \bar{w}_k . Proper treatment of this term comprises most of the difficulty in LES subgrid modeling. The difficulty results from the often highly nonlinear behavior of the rate expression used to describe \dot{w}_k . Subgrid fluctuations in species and temperature play a significant role in this term. For example, Frankel *et al.* (1993) showed that neglecting these fluctuations produced large errors in reacting mixing layer simulations.

Among the most comprehensive approaches to approximating \bar{w}_k are the assumed pdf method of Frankel *et al.* (1993) and the pdf evolution equation method of Gao and O'Brien (1993). The assumed pdf method specifies subgrid species mixing in terms of an assumed pdf shape which is a function of, at minimum, second order correlations of the species such as $(\tilde{Y}_k \tilde{Y}_k - \tilde{Y}_k \tilde{Y}_k)$. These correlations must be predicted from equations which are difficult to model. Frankel *et al.* (1993) cited the inadequacies in the prediction of the high order species correlations as a primary source of disagreement of the assumed pdf method with DNS data.

The pdf evolution equation method of Gao and O'Brien (1993) is a more general alternative but has not yet been fully developed and applied. A primary difficulty in this approach is the accurate modeling of the subgrid molecular mixing terms appearing in the pdf equation. Proper modeling of this term has consistently been a stumbling block in pdf methods. This problem is exacerbated by the fact that the coupling of small scale stirring and molecular diffusion in turbulent reacting flows is one of the most important effects.

An alternative approach to modeling the combustion related subgrid terms is to use the LEM model of Kerstein as a subgrid model in LES. The next section gives a brief description of the LEM model before its implementation into LES is described.

3 LINEAR-EDDY MODEL

The LEM model has been described extensively by Kerstein (1988, 1989, 1990, 1991, 1992) and is therefore only briefly discussed here. This model is designed to separately treat two fundamental physical processes which describe the evolution of chemical species in turbulent flames. These two processes are molecular diffusion and turbulent convective stirring. Molecular diffusion is treated within the model deterministically by the numerical solution of the species and temperature diffusion equations (Calhoun *et al.*, 1995) which include the effects of chemical reactions. Turbulent stirring, however, is modeled stochastically by a series of instantaneous rearrangement events of the species and temperature fields. These rearrangement events correspond to mixing induced by turbulent eddies. The length scale and frequency of these eddies are determined from relationships derived by Kerstein (1992). These relationships

were derived by equating the diffusivity of a random walk of a fluid particle under the influence of the rearrangement events with the scaling of turbulent diffusivity.

The strategy employed within the LEM model is to resolve all relevant fluid mechanical length scales of the flow, as in direct numerical simulations. As a result, the reaction rate terms in the species and temperature equations appear in closed form and do not require additional modeling. Resolving all length scales of the flow, however, will in general be computationally intractable in the foreseeable future. As a result, the LEM model is implemented in only one spatial dimension to keep the simulations affordable.

One underlying assumption in the model is constant pressure. As a result, the LEM fluid elements will necessarily expand with temperature increase. This expansion will cause a decrease in the local scalar gradients in the vicinity of the flame and thereby a reduction in molecular diffusion. Algorithms for the implementation of volumetric expansion within the LEM model have been described by Kerstein(1991) and Goldin and Menon(1996). In this study, however, heat release is assumed to be low so that volumetric expansion may be neglected.

Inputs for the LEM model are the integral length scale L_{LEM} , the model Reynolds number Re_{LEM} , pressure, the species molecular diffusivities, thermal conductivity λ , species specific heats $c_{p,k}$ and the reaction rate constants. With specification of appropriate initial and boundary conditions, the species and temperature fields evolving in homogeneous, stationary turbulence can be determined(see McMurty *et al.*(1993) for a description of the nonreacting mixing case). These fields can be used to directly compute subgrid temperature and species correlations needed for the LES simulation. One striking advantage of this approach over other formulations is the explicit inclusion of Reynolds number and molecular diffusivities in the model.

4 LEM SUBGRID MODEL

The LEM model may be used as a subgrid model for the small unresolved scales of the flow while the larger scales are calculated directly from the LES equations of motion. This approach requires the prescription of a method to couple the 1-D LEM model with the multi-dimensional LES resolved field equations. At present, there are two ways to accomplish this task. The first is called the *LEM pdf specification*(LEMS) approach. This is an extension to LES of the work of Goldin and Menon(1996) for the Reynolds averaged Navier-Stokes equations. The second approach is termed the *LEM pdf calculation*(LEMC) approach. The LEMC method was first developed by Menon *et al.*(1993b) in the context of premixed flames. It has also been applied to describe diffusion flame structure by McMurty *et al.*(1992).

The LEMS approach, though very useful, employs the use of the gradient diffusion assumption to model $\Phi_{k,j}^{sgs}$ as described above. The LEMC approach, on the other hand, avoids this assumption completely. As a consequence, the

remainder of this study is concerned only with the LEMC approach. The LEMS procedure is described and discussed in Calhoun(1996). The LEMC method has been described in detail by Menon *et al.*(1993b), McMurty *et al.*(1992) and Calhoun(1996). As a result, LEMC the method is only outlined and the proposed improvements to the algorithm noted here for brevity.

The strategy adopted in the LEMC approach is to explicitly implement a 1-D LEM spatial domain within the subgrid of each LES grid cell. Given the processes that effect the LEM subgrid fluid elements, the evolution of the subgrid species and temperature fields and their associated subgrid joint pdf is then calculated directly during the LES simulation. This scheme is therefore denoted the *LEM pdf calculation* procedure.

The LEMC procedure seeks to model all the processes, both large and small scale, which influence the evolution of the subgrid Y_k fields. As a result, the filtered species \bar{Y}_k may be calculated directly by filtering the subgrid Y_k fields. This obviates the need to solve the LES filtered equations for \bar{Y}_k . Consequently, use of conventional models for $\Phi_{k,j}^{sgs}$ employing the gradient diffusion assumption is completely avoided. Within the LEMC approach, modeling of the small scale processes is accomplished using the LEM model. The Y_k fields are also influenced by large scale convection. This process is modeled by employing a modified version of the "splicing" algorithm developed by Menon *et al.*(1993b) which convects subgrid fluid elements from one LES cell to another.

The processes effecting the evolution of the subgrid scalar fields are 1) molecular diffusion, 2) chemical reaction, 3) subgrid turbulent stirring and 4) large scale convection. These processes can be characterized by the time scales Δt_{diff} , Δt_{chem} , Δt_{stir} and Δt_{conv} respectively. Given these time scales, the temporal evolution of the subgrid scalar fields is represented within the LEMC procedure as follows. Given the initial subgrid scalar fields in each LES cell, the processes of molecular diffusion, chemical reaction, turbulent stirring and large scale convection are implemented as discrete events occurring in time. The epochs of these events are determined by the respective time scales of each process. This type of discrete implementation is similar to the fractional step method used to solve differential equations.

As the subgrid T and Y_k fields evolve under the action of these processes, the LES equations for $\{\bar{\rho}, \bar{\rho}u_j, \bar{\rho}\bar{E}\}$ are also solved concurrently on the acoustic time scale Δt_{LES} . The subgrid scalar fields are coupled to the resolved scales in the following ways. First, the subgrid length scale L_{LEM} is specified equal to the LES characteristic filter size Δ_{LES} . Second, LEM model Reynolds number Re_{LEM} is specified in terms of k^{sgs} as $Re_{LEM} = \sqrt{k^{sgs}}L_{LEM}/\nu$ with ν being the kinematic viscosity based on the resolved field. Third, the subgrid molecular diffusivities, thermal conductivity, specific heats and reaction rate constants are set equal to the resolved field values. Fourth, the resolved species mass fractions \bar{Y}_k are calculated by a direct filtering of the sub-

grid fields. Finally, the subgrid T field may be coupled to the resolved scales as described by Menon *et al.*(1993a) or by a modified scheme described by Calhoun(1995). In this study, however, heat release is assumed negligible so that the subgrid T is equal to the resolved value \bar{T} . This completes the outline of the method. Modifications to the algorithm originally proposed by Menon *et al.*(1993b) and McMurtry *et al.*(1992) are described below.

The LEM model requires boundary and initial conditions for the subgrid diffusion equations to be specified. In previous applications of the LEMC method, the subgrid LEM spatial coordinate s was assumed to be periodic. In this study, however, zero gradient boundary conditions are used on both Y_k and T . These conditions are consistent with the notion that species and heat diffusion at the large scales(i.e. scales of the order of Δ_{LES} and larger) are negligible for high Re flows. Initial conditions for subgrid fields are determined from the splicing or large scale convection events occurring on the time scale Δt_{conv} . Each splicing event transfers subgrid fluid elements from one LES cell to another generating new Y_k and T distributions which then evolve as prescribed by the LEM model.

The subgrid integral length scale L_{LEM} has been specified equal to the local characteristic filter size Δ_{LES} as in previous LEMC implementations. It should be recognized, however, that L_{LEM} plays an important role in subgrid mixing. L_{LEM} determines the magnitude of the subgrid scalar gradients and the diffusion time scale Δt_{diff} . L_{LEM} also determines Re_{LEM} which in turn prescribes the subgrid stirring time scale Δt_{stir} . Taking $L_{LEM} = \Delta_{LES}$ may not be appropriate because the LEM spatial coordinate s has been interpreted by Kerstein(1991) as a space curve aligned with the local scalar gradients. L_{LEM} may therefore be much longer than Δ_{LES} . The lack of a precise definition of L_{LEM} results in the need to calibrate the mixing model. Calibration of the model is also necessary because coefficients in the expressions of other subgrid LEM parameters have been set to one, following historical precedent.

In order to calibrate the mixing model, L_{LEM} could be specified, for example, as Δ_{LES} times some calibration coefficient. Another approach is to specify new time scales for the diffusion and stirring processes in the LEM model as,

$$\Delta t_{diff}^* = C_\tau \Delta t_{diff} \quad (4)$$

$$\Delta t_{stir}^* = C_\tau \Delta t_{stir} \quad (5)$$

where C_τ is a calibration coefficient and Δt_{diff} and Δt_{stir} are specified taking $L_{LEM} = \Delta_{LES}$. Equations (4) and (5) result from recognizing that L_{LEM} determines the temporal rate of mixing. Use of these equations rescales the time coordinate of the subgrid diffusion and stirring processes to match those of the condition chosen to calibrate the model. This time scaling approach, however, is not applied to the chemistry. The chemical processes are not explicitly a function of the subgrid length scale and should therefore

have the same temporal coordinate as the LES resolved field equations.

A similar time scaling procedure was implemented by McMurtry *et al.*(1993) who used the LEM model to predict passive scalar mixing in homogeneous, stationary turbulence. Other mixing models employed in various schemes also include calibration coefficients. These coefficients may appear explicitly(e.g. pdf mixing model closure) or implicitly through other models which influence species mixing(e.g. eddy viscosity models for $\Phi_{k,j}^{sgs}$).

Other modifications to the original algorithm of Menon *et al.*(1993b) and McMurtry *et al.*(1992) deal with the large scale convection or splicing algorithm. This algorithm is discussed in detail by Menon *et al.*(1993b) and is only briefly described here. This algorithm moves subgrid fluid elements from one LES cell to another based on the local velocity field u_j . The local velocity consists of the resolved velocity \bar{u}_j plus a fluctuating component u_j'' . The resolved velocity is calculated from the LES equations while the fluctuating component is estimated in terms of k^{sgs} similar to Menon *et al.*(1993b). The splicing events are implemented discretely in time on the time scale Δt_{conv} . Each splicing event involves several steps which are: (1) determination of volume transfer between adjacent LES grid cells, (2) identification of the subgrid elements to be transferred given the volume transfer, and (3) splicing of the identified fluid elements across LES cell boundaries into the subgrid LEM domains.

Step (1) of the splicing process has been modified from that suggested by Menon *et al.*(1993b) in two ways. First, the volume transfers due to both \bar{u}_j and u_j'' are calculated in a conservative manner. The previous algorithm calculated these transfers nonconservatively which may result in significant mass conservation errors. Second, the contributions from both \bar{u}_j and u_j'' are treated as a single volume transfer. Menon *et al.*(1993b) treated these contributions separately which may result in a nonphysical upstream propagation of species.

Step (2) of the algorithm has also been modified. This step involves 1) calculating the number of subgrid fluid elements to be transferred given the volume fluxes between LES cells, and 2) identifying which specific elements are to be transferred. The number of elements to be transferred is calculated here as described by Menon *et al.*(1993b). The manner in which elements are chosen for transfer, however, has been modified. Menon *et al.*(1993b) chose these elements in a random fashion in order to model the random behavior of turbulent transport. In this study, however, these subgrid elements are specified in an ordered fashion. This is done so that the splicing algorithm may recover laminar convection when the turbulent kinetic energy is zero. The previous splicing algorithm does not have this property.

To describe how the subgrid transfer elements are chosen, first recall that in this study the LEM domain has a length L_{LEM} and is *not* periodic in s . Here, the $s = 0$ and $s = L_{LEM}$ extremities of the domain are interpreted

as inflow and outflow boundaries, respectively, of the subgrid with neighboring LES grid cells. With this interpretation, the outgoing subgrid elements are chosen from the $s = L_{LEM}$ end of the domain while incoming elements enter from the $s = 0$ end. Step (3) of the splicing algorithm accomplishes the actual transfer of subgrid elements. This inflow/outflow interpretation results in elements entering a LEM domain from the $s = 0$ boundary. They are then convected through the domain and out the $s = L_{LEM}$ boundary by successive splicing events. During this "flow through" process, subgrid fluid elements, and their associated Y_k and T values, are stirred, diffused, etc. by the LEM model. This new ordered splicing approach eliminates the conservation error described by Menon *et al.*(1993b) of the previous random algorithm.

One artifact of the splicing algorithm implemented here and in the approach of Menon *et al.*(1993b) is the generation of discontinuities in the subgrid fields. These discontinuities appear between the incoming subgrid elements and the original field. As noted by McMurtry *et al.*(1992), these discontinuities are unphysical and result in spurious diffusion in their vicinity. Previously, this error was neglected. In this study, however, this error is removed by not allowing diffusion across these discontinuities. The subgrid domain is then effectively partitioned into sub-subgrid domains. This partitioning only affects the solution of the diffusion equations and has no effect on the subgrid stirring events. The subgrid stirring process may overlap the subgrid partitions transferring species from one partition to another.

The splicing algorithm described here has the important property that species convection is treated in a similar manner as in Lagrangian schemes. That is, convection is independent of the magnitude or gradient of the species which are transported. Convection in the splicing algorithm only depends on the velocity field. As a result, subgrid elements are transported without changing their species and temperature magnitudes. This property allows the splicing algorithm to avoid the classic difficulty of false numerical diffusion associated with the numerical approximation of convective terms in differential equations. By avoiding numerical diffusion, and also the gradient diffusion assumption, the splicing algorithm allows an accurate picture of the small scale effects of molecular diffusion to be captured, including differential diffusion effects.

5 NUMERICAL FORMULATION

The modeled LES equations for $\{\bar{\rho}, \bar{\rho}u_j, \bar{\rho}\tilde{E}\}$ are solved numerically in finite volume form. The inviscid cell face fluxes are approximated using the AUSM flux split scheme(Liou and Steffen, 1993) extended to fifth order using the MUSCL approach. The fifth order interpolation is upwind-biased with a stencil given by Hariharan and Sankar(1994). The viscous stresses and heat flux terms are evaluated with the fourth order scheme of Bayliss *et al.*(1985). All other spatial derivatives in the LES equations are approximated to

fourth order using central differences. Time advancement is accomplished using a second order Rugga-Kutta scheme. The pressure gradient scaling technique of Ramshaw *et al.*(1985) is used to ensure temporal stability of the scheme for a fixed time step Δt_{LES} . The time steps specified in all simulations, however, correspond to a *CFL* number of $\approx .3$.

The subgrid LEM diffusion equations are discretized using second order central differences on an equally spaced grid. The grid spacing is specified as $\Delta s = L_{LEM}/N_{LEM}$ where N_{LEM} is the number of subgrid fluid elements. The subgrid equations are time advanced using the backward Euler scheme. The time scales Δt_{diff} and Δt_{chem} are specified from stability considerations with *CFL* numbers of .25 and $\approx .01$ respectively. The time scale Δt_{stir} of the LEM model is specified following Menon *et al.*(1993b) with $L_{LEM} = \Delta_{LES}$. The velocity time scale of the splicing algorithm is specified as,

$$\Delta t_{conv} = \frac{\prod_i \Delta x_i}{|\varepsilon_{i,j,k}| \tilde{u}_i \Delta x_j \Delta x_k} \quad (6)$$

where Δx_i is the grid cell width in the i th coordinate direction and $\varepsilon_{i,j,k}$ is the Levi-chi-vita tensor.

Several DNS test cases were conducted in order to validate the implementation of the AUSM discretization. The LDKSGS subgrid model was also validated by comparing LES simulations of decaying isotropic turbulence with DNS data. The subgrid discretization was validated with an exact solution of the diffusion equation. It should also be noted that a test conducted using a sixth order compact scheme to solve the diffusion equation showed only a small improvement over the second order central difference scheme. As a result, the second order scheme was adopted due to its simplicity. The splicing algorithm implementation was also validated through a series of convection tests.

6 MODEL APPLICATION: REACTING MIXING LAYER

This section describes the application of the LEMC subgrid approach to the LES modeling of mixing and reaction in high Reynolds number mixing layers. The combined modeling approach will be denoted the LES-LEMC method. Reacting mixing layers have been extensively studied experimentally for a wide range of conditions(see Dimotakis(1989) for a recent review). The results of these experiments provide an opportunity to demonstrate the capabilities of the LES-LEMC approach. In this initial study, the simulations are restricted to temporally evolving layers in only two spatial dimensions. The 2-D assumption may be justifiable because experiments have shown the early stages of development of many mixing layers to be dominated by large two dimensional coherent structures(Roshko, 1976; Dimotakis, 1989). These structures may also persist to considerable downstream distances. Three dimensional mixing in the early stages occurs at the

small scales. Further downstream, however, 3-D mixing becomes a dominant effect.

Within the 2-D application of the LES-LEMC approach, the development of the large scale coherent structures in the mixing layer are modeled by the LES resolved field equations. The 3-D small scale mixing effects are modeled by the LEMC subgrid approach which relies on the LEM mixing model. The LEM model, though only a 1-D approximation, has been shown to capture 3-D mixing effects in homogeneous, stationary turbulence (McMurty *et al.*, 1993). This 2-D large scale/3-D small scale formulation of the LES-LEMC method may therefore provide a realistic representation of the early stages of development of physical mixing layers. This formulation also makes it possible to predict the post turbulent transition behavior of high Reynolds number layers. This is unattainable in a purely 2-D simulation because there is no mechanism for 3-D small scale mixing.

The simulations presented here seek to model mixing layers with dilute reactant species and low heat release reactions. Within this restriction, several simplifying assumptions are made. To begin with, Fickian diffusion with equal diffusivities for all species is assumed. With this assumption the mixing process can be completely described in terms of the Shvab-Zeldovich mixture fraction ξ (Williams, 1985). ξ is the normalized mass fraction of an atomic species originating in the fuel stream. ξ is therefore one in the fuel stream and zero in the oxidizer stream. The LEM subgrid diffusion equation for ξ is given by,

$$\frac{\partial \xi}{\partial t} = \frac{1}{\rho} \frac{\partial}{\partial s} \left(\rho D \frac{\partial \xi}{\partial s} \right) \quad (7)$$

where the diffusion coefficient is taken as $D = \nu / Sc$. The Schmidt number Sc for all simulations is set equal to .7 which is characteristic of gases. The unreacted species in the subgrid are linearly related to ξ and can be found given their values in the fuel and oxidizer streams. With D given as above, the Lewis number, $Le = \lambda / \rho c_p D$, is also assumed to be equal to one.

The reaction chemistry in the layer is assumed to be governed by the elementary irreversible reaction $F + O \rightarrow P$. This reaction is also taken to have negligible heat release. This allows the subgrid temperature equation to be eliminated from the LEM formulation. The subgrid temperature is then specified equal to the LES resolved temperature \bar{T} . The subgrid correlations T_k^{sgs} and $T_k^{sgs,n}$ in the state equations are then zero.

Both the cases of infinite and finite reaction rate are considered. For infinite rate chemistry, the product formation can be calculated given ξ by assuming complete conversion of all reactant species. For the finite rate case, equation (7) must be supplemented by an equation to describe the product formation given by,

$$\frac{\partial Y_P}{\partial t} = \frac{1}{\rho} \frac{\partial}{\partial s} \left(\rho D \frac{\partial Y_P}{\partial s} \right) + \frac{\dot{w}_P}{\rho} \quad (8)$$

with,

$$\dot{w}_P = A_P \rho^2 Y_F Y_O \quad (9)$$

where the rate A_P is assumed constant. Y_F and Y_O are calculated from the mixture fraction as,

$$Y_F = \xi Y_{F,o} - \frac{Y_P}{2} \quad (10)$$

$$Y_O = (1 - \xi) Y_{O,o} - \frac{Y_P}{2} \quad (11)$$

where $Y_{F,o}$ and $Y_{O,o}$ are the mass fraction values of F and O in the fuel and oxidizer streams respectively. These expressions assume the species molecular weights are $W_F = W_O = \text{constant}$ and $W_P = 2W_F$ by atom conservation.

The reactant species in the model problem are diluted in an inert fluid. This fluid is assumed to have the thermodynamic properties of air so that,

$$c_p = \sum_{k=1}^K c_{p,k} Y_k \cong c_{p,air} \quad (12)$$

and similarly for the other properties except for the viscosity. The viscosity is taken as a constant specified in terms of Reynolds number. The thermal conductivity λ is then specified given the Prandtl number Pr equal to .72. Specifying the thermodynamic properties in this manner and neglecting heat release decouples the fluid dynamics from the chemistry.

The computational domain for all simulations is a $H \times (H + \Delta H)$ box where $H = 2\pi$. Periodic boundary conditions are applied in the streamwise x_1 direction while slip wall conditions are applied at $x_2 = \pm(H + \Delta H)/2$. The grid is equally spaced on the range $-H/2 \leq x_1 \leq H/2$ and $-H/2 \leq x_2 \leq H/2$ with $\Delta x_1 = \Delta x_2 = H/N_{LES}$. For $H/2 \leq |x_2| \leq (H + \Delta H)/2$, the grid is stretched and the AUSM scheme is reduced from fifth to third order. This grid stretching and order reduction of the scheme are used in order to damp acoustic reflections from the upper and lower slip wall boundary conditions. The upper and lower boundaries are also set far enough away so that the simulations model unconfined mixing layers. N_{LES} for all simulations is 128. The stretched portion of the grid contains 20 additional points on both the top and bottom which are distributed using a stretching factor of 1.5.

The subgrid LEM resolution N_{LEM} is chosen based on the criteria that the smallest length scales of the flow be resolved. With $Sc = .7$, the Batchelor scale is larger than the Kolmogorov scale η_K . The LEM grid is then specified assuming a minimum resolution of six subgrid elements per Kolmogorov scale. η_K is estimated from the scaling relation $L_{LEM}/\eta_K = Re_{LEM}^{3/4}$. This resolution requirement is checked throughout the simulations to ensure the quality of the solution. A subgrid resolution of $N_{LEM} = 300 - 600$, depending on the specific simulation, was found to adequately resolve η_K . For the mixing layer simulations, the largest value of Re_{LEM} in the domain occurs in the early times and decays as the simulation proceeds. As a result,

the resolution of η_K in the subgrid improves throughout the simulation. It should also be noted that with proper resolution of η_K the subgrid scalar statistics will be converged. This results from the fact that no additional scalar fluctuations will exist below η_K . However, if Sc were greater than one, the resolution requirement would be based on the Batchelor scale.

The resolved velocity field \tilde{u}_j is initialized as a mean field plus a perturbation. The mean velocity is specified by,

$$\begin{aligned}\langle u_1 \rangle_{mean} &= \frac{U_o}{2} \tanh(x_2/\alpha) \\ \langle u_2 \rangle_{mean} &= 0\end{aligned}\quad (13)$$

where $\langle M \rangle_{mean}$ denotes the mean value of M averaged in the periodic direction. U_o is the velocity difference across the layer and α is a constant related to the initial vorticity thickness $\delta_{\omega,o}$. The vorticity thickness is defined by,

$$\delta_{\omega} = U_o \left[\frac{\partial \langle u_1 \rangle_{mean}}{\partial x_2} \right]_{max}^{-1} \quad (14)$$

Applying this definition to $\langle u_1 \rangle_{mean}$ in equation (13) yields $\delta_{\omega,o} = 2\alpha$. In all the simulations presented in this study $\alpha = .1496$. From linear stability analysis (Michalke, 1964), this value of α causes the third spatial mode of the layer to be the most unstable.

The perturbation velocity added to $\langle u_j \rangle_{mean}$ is specified in a similar manner to Riley and Metcalfe (1980). The perturbation is taken as an isotropic velocity field with an energy spectrum which decays as k^{-2} where k is the magnitude of the spectral wave number vector k_j . This velocity field is then modified by a form function which preserves the divergence free property and gives a streamwise velocity fluctuation $\langle u_1 \rangle_{rms}$ of the form (Riley and Metcalfe, 1980),

$$\frac{\langle u_1 \rangle_{rms}}{U_o} = .18 \exp(-.147(2x_2/\delta_{1/2})^2) \quad (15)$$

where $\delta_{1/2}$ is the velocity half width of $\langle u_1 \rangle_{mean}$.

U_o for all simulations is set to 71 m/sec, except where noted. This corresponds to a Mach number of .2. The resolved pressure \bar{p} and temperature \bar{T} are initialized constant in the computational domain and equal to 1 atm and 300K respectively. Based on these conditions, the viscosity is set so that $Re_{\omega,o} = U_o \delta_{\omega,o} / \nu = 7000$. The subgrid kinetic energy is initialized using the approximation (Kim and Menon, 1995),

$$k^{sgs} \cong C_K k^{res} \quad (16)$$

where C_K is a constant and k^{res} is given by $k^{res} = (\tilde{u}_i \tilde{u}_i - \tilde{u}_i \tilde{u}_i) / 2$. \tilde{u}_i is the resolved velocity explicitly Favre filtered on the filter size $2\Delta_{LES}$. Kim and Menon (1995) derived an expression for C_K and found it to have a value of approximately .45 for 3-D stationary isotropic turbulence. This value is also adopted in this study.

Since heat release is neglected, the LEM subgrid density is set equal to its corresponding LES filtered value $\bar{\rho}$ initially and throughout the simulation. The subgrid mixture

fraction is similarly initialized as constant in each LES cell and equal to a mean value specified by,

$$\langle \xi \rangle_{mean} = \frac{1}{2} (1 + \tanh(x_2/\alpha)) \quad (17)$$

For the case of finite reaction rate chemistry, the product field Y_P is initialized to zero following McMurtry *et al.* (1989).

The final parameter to be specified is the LEMC time scaling coefficient C_τ . This coefficient is specified as $C_\tau = 100$ for all simulations. The reasoning behind this choice will be discussed below.

7 RESULTS AND DISCUSSION

7.1 INFINITE RATE CHEMICAL REACTION

As mentioned above, by assuming negligible heat release and dilute reactant species, the fluid dynamics become decoupled from the subgrid scalar fields. The velocity field therefore evolves in the same manner for both the infinite and finite reaction rate cases. Consequently, the evolution of the velocity field is discussed only in this section.

Figure 1 shows a plot of the growth of the k_1 modal energies E_{k_1} of the mixing layer during the simulation. The modal energies are calculated by integrating the spectral energy in the periodic direction across the layer as,

$$E_{k_1} = \int_{-(H+\Delta H)/2}^{+(H+\Delta H)/2} \hat{u}_i(k_1) \hat{u}_i^*(k_1) dx_2 \quad (18)$$

where \hat{u}_i and \hat{u}_i^* are the Fourier transform of the i th component of the filtered velocity and its complex conjugate respectively. Time in the figure is nondimensionalized by $\delta_{\omega,o}/U_o$. From the figure, the third mode of the layer begins to grow rapidly shortly after the start of the simulation. The first and second modes, however, do not exhibit significant growth until somewhat later times. This behavior results from the initialization in which the third mode was set as the most unstable from linear stability analysis (Michalke, 1964). It is also apparent that both the second and third modes have linear growth regions as expected for unconfined mixing layers. The third mode saturates at $\tau \simeq 20$ and begins to lose energy. By the end of the simulation, the second mode is dominant but with significant energy in the first mode as well.

Vorticity contours, not shown here, show that at $\tau \simeq 19$ there are three well defined structures in the layer which are approximately colinear. Further in the simulation these structures begin to pair as the first and second modal energies become significant. Vorticity contours also show the smaller structures of the layer becoming more obscure as the simulation continues. This is consistent with DNS simulations of 2-D, decaying isotropic turbulence (Fornberg, 1977; McWilliams, 1984) in which isolated vorticity concentrations developed. This behavior occurs by a process

in which energy is transferred to the large scales while enstrophy is transferred to smaller scales where it is dissipated (McWilliams, 1984).

The streamwise velocity field evolves self-similarly as is expected for unconfined mixing layers. Figure 2 shows a plot of the mean velocity $\langle \tilde{u}_1 \rangle_{mean}$ across the layer plotted in terms of the similarity coordinate x_2/δ_m . δ_m is the momentum thickness defined by,

$$\delta_m = \int_{-\infty}^{+\infty} \frac{\langle \tilde{p} \rangle_{mean}}{\tilde{\rho}|_{x_2=+\infty}} U^* (1 - U^*) dx_2 \quad (19)$$

where,

$$U^* = \frac{\langle \tilde{u}_1 \rangle_{mean} - \tilde{u}_1|_{x_2=-\infty}}{\tilde{u}_1|_{x_2=+\infty} - \tilde{u}_1|_{x_2=-\infty}} \quad (20)$$

The predicted mean velocity has also been averaged in time for $\tau \geq 5$. Included in the figure is the experimental data of Bell and Mehta (1990) who measured the velocity profile in a turbulent mixing layer at several downstream locations. As seen in the figure, the predicted velocity profile is in excellent agreement with the experiment data.

The simulation is at a high enough Reynolds number to be beyond the mixing transition. The mixing transition is characterized by the appearance of small scale 3-D motions which significantly increase mixing and product formation above that obtained for pre-transition mixing layers. From the data of Koochesfahani and Dimotakis (1986), the mixing transition is complete by $Re_\omega \simeq 7000$. Figure 3 shows a plot of Reynolds number evolution in time. Several values of Re based on different transverse length scales are shown. The velocity scale of these Reynolds numbers is U_o . The viscosity μ is a constant equal to the reference value and the density is taken as the domain averaged value.

The length scales for the different values of Re in Figure 3 are the vorticity (δ_ω), momentum (δ_m), mixture fraction (δ_ξ) and mixed probability (δ_{P_m}) thickness. δ_ω and δ_m are defined above in equations (14) and (19). However, the velocity in equation (14) must be replaced with the filtered value since u_1 is not known from the LES equations. The mixture fraction thickness δ_ξ is defined as the width of the region $.01 \leq \langle \xi \rangle_{mean} \leq .99$. $\langle \xi \rangle_{mean}$ may be calculated by directly averaging the subgrid LEM ξ field avoiding the spatial Favre filtering in the expressions for δ_ω and δ_m . The mixed probability thickness is calculated as the width of the region $\langle P_m \rangle_{mean} \geq .99$ where $\langle P_m \rangle_{mean}$ is the mean mixed fluid probability defined by (Koochesfahani and Dimotakis, 1986),

$$\langle P_m \rangle_{mean} = \int_\epsilon^{1-\epsilon} \langle p^{gs}(\xi) \rangle_{mean} d\xi \quad (21)$$

$\langle p^{gs} \rangle_{mean}$ is the mean subgrid mixture fraction pdf calculated from all the subgrid fields at a particular x_2 station. Note that the integral in equation (21) excludes the pure unmixed fluid outside the range $\epsilon \leq \xi \leq 1-\epsilon$. In this study ϵ is taken as .033.

As seen in Figure 3, Re_ω evolves from an initial value of 7000 and increases in time. As a result, the entire simulation is beyond the mixing transition. Also note from

the figure that the different length scales grow approximately linearly after an initial development period. This linear growth is characteristic of self-similar mixing layers. Re_{P_m} is found to be more sensitive to the evolution of the subgrid fields than Re_ξ due to the sensitivity of $\langle P_m \rangle_{mean}$ to intermittency at the edge of the layer. δ_{P_m} exhibits a longer development region than δ_ξ and begins approximate linear growth by $\tau \simeq 7$. At the end of the simulation the growth of all length scales taper off due to the saturation of the $k_1 = 3$ mode shown in Figure 1. Further in time, linear growth will resume as the energy of the $k_1 = 2$ mode grows (Figure 1) and the primary vortices pair. Figure 3 also shows that the linear growth rates of δ_ξ and δ_{P_m} are approximately twice the rate of δ_ω . This is in agreement with experimental data of Brown and Roshko (1974) noting that δ_ξ and δ_{P_m} are comparable to the visual thickness (Brown and Roshko, 1974; Koochesfahani and Dimotakis, 1986) commonly measured in experimental investigations.

The relatively large values of global mixing layer Re in Figure 3 translate into large subgrid Reynolds number Re_{LEM} . As discussed above, Re_{LEM} is used to determine the required resolution in the subgrid based on the criteria that at least six subgrid elements are needed to resolve η_K . Given this criteria and the Kolmogorov scaling relation for η_K , a relationship for the required subgrid resolution can be derived as $N_{LEM,min} = 6(Re_{LEM,max})^{3/4}$. Figure 4 presents a plot of $N_{LEM,min}$ calculated over the entire domain as a function of time. Initially $N_{LEM,min} \simeq 313$ and begins to drop quite rapidly shortly after the start of the simulation. $N_{LEM} = 400$ has been used for this simulation so that the subgrid is well resolved. Using $N_{LEM} = 300$, however, would be adequate for this simulation because only two LES cells in the entire domain were found to contribute to N_{LEM} being greater than 300. Figure 4 also shows $N_{LEM,min}$ to exhibit an approximate power law decay as the simulation continues. This is related to the decay of Re_{LEM} in the layer which results from the decay of k^{gs} . Figure 5 shows a plot of the evolution of the total mean subgrid kinetic energy k_{tot}^{gs} in time. k_{tot}^{gs} is defined by,

$$k_{tot}^{gs} = \int_{-\infty}^{+\infty} \langle k^{gs} \rangle_{mean} dx_2 \quad (22)$$

After a short development period, k_{tot}^{gs} shows a power law decay as indicated by the linear slope in Figure 5 after $\tau \simeq 1$. This behavior of k_{tot}^{gs} is due to the self-similarity of the layer.

Turning now to the evolution of the chemically reacting fields, several cases were considered in which the concentration of the reactants were varied in the fuel and oxidizer streams. These cases were specified in terms of the equivalence ratio ϕ defined by Mungal and Dimotakis (1984) (hereafter referred to as M-D). ϕ is the ratio of the low speed side reactant concentration to the high speed reactant concentration, divided by the stoichiometric low speed to high speed reactant concentration ratio. For the simulations in this study, the high speed side is

taken as the upper side of the layer carrying species F . For the elementary reaction considered here, the stoichiometric ratio of F to O is equal to one. Recalling that $W_F = W_O$ and that the diluent properties are the same on both sides of the layer, ϕ reduces to,

$$\phi = \frac{Y_{O,o}}{Y_{F,o}} \quad (23)$$

The values of ϕ considered in this study are given in Table 1. This table also gives the corresponding stoichiometric values of mixture fraction and product mass fraction for each case (the subscript "st" denotes the stoichiometric value). These cases correspond to the experiments of M-D who investigated hydrogen-fluorine reaction in a turbulent gaseous mixing layer. The reactants in these experiments were sufficiently diluted in an inert fluid so that the chemistry did not effect the evolution of the velocity field (Mungal and Dimotakis, 1984).

Table 1

Infinite rate cases		
ϕ	ξ_{st}	$Y_{P,st}$
1/8	.111	.0178
1/4	.200	.0160
1/2	.333	.0133
1	.500	.0100
2	.667	.0133
4	.800	.0160
8	.889	.0178

For reacting mixing layers Mungal *et al.* (1985) showed that the product field does not evolve self-similarly due to a Reynolds number dependence of the mean product. This result also implies that the mixture fraction pdf is also not self-similar because Mungal *et al.*'s experiments were conducted in the limit of fast chemistry (Mungal *et al.*, 1985). As a result, time averages of Y_P and ξ may not be calculated as done for the velocity field in Figure 2. Only spatial averages at instants in time are relevant.

Figure 6 shows the spatial averaged values of Y_P across the layer at a time of $\tau = 19$ for the cases listed in Table 1. The transverse coordinate has been nondimensionalized by δ_{Pm} . The fuel stream in this figure is on the $x_2 \rightarrow +\infty$ side and the oxidizer on the $x_2 \rightarrow -\infty$ side. The time of $\tau = 19$ is in the linear growth region shown in Figure 3 and just prior to the saturation of the $k_1 = 3$ spatial mode seen in Figure 1. At this time there are three well defined large scale structures which are approximately colinear. The product profiles in Figure 6 exhibit several qualitative trends observed in the experiments of M-D. First, the profiles are asymmetric for $\phi \neq 1$ and skewed toward the side of the layer which is lean in freestream reactants. For $\phi < 1$ the profiles are biased to the lower side and for $\phi > 1$ toward the upper side. Second, as $\phi \rightarrow 1$, the profiles increasingly become more symmetric until at $\phi = 1$ the mean product is approximately symmetric. The data of M-D, however, showed the peak value for $\phi = 8$ to be much

larger than for $\phi = 1/8$ where Figure 6 shows these values to be approximately the same. This disagreement reflects the difference in the entrainment ratio (Dimotakis, 1989) of fluid into the layer for the present temporal simulation and for the experiments. The entrainment ratio E_T is the ratio of the volume of high speed to low speed fluid drawn into the layer. M-D estimated their layer to have $E_T = 1.3$. Temporal simulations, however, are known to entrain fluid in a symmetric manner so that $E_T = 1$ (Dimotakis, 1989).

Figure 7 is a re-plot of the data in Figure 6 normalized by the stoichiometric values of Y_P given in Table 1 for each value of ϕ . This figure shows the peak mean product to be a maximum for $\phi = 1$ and to drop off for $\phi \neq 1$. This trend was also observed by M-D. They found the maximum peak product to occur for ϕ equal to the entrainment ratio and to be less for ϕ off this condition. The peak values of mean product from the present simulations are in the range $.57 \leq (Y_P)_{mean}/Y_{P,st} \leq .65$. This range is in good agreement with that measured by M-D of $.54 \leq (Y_P)_{mean}/Y_{P,st} \leq .67$. The range predicted from the simulations is slightly narrower than for the experiment, again reflecting the difference in entrainment ratio. Figure 7 also shows the shift of the peak values for $\phi = 1/8$ to $\phi = 8$ to span approximately 25% of the layer width, in agreement with M-D.

Figure 8 shows a direct comparison of the present results for mean product at $\phi = 1$ to the experimental results of M-D for two different runs. The experimental product data has been calculated from the measured mean temperature profiles as described by M-D. The agreement between the present simulation and the experiment is quite good. The peak value as well as the shape of the profile have been captured in the simulation. The data of M-D is for a mixing layer at a comparable but slightly larger Reynolds number. $Re_{Pm} = 6.5 \times 10^4$ for the experiment and $\simeq 4.1 \times 10^4$ for the simulation. The product formation in a turbulent mixing layer is known to be a function of Re (Mungal *et al.*, 1985). However, it is a slow function of Re (approximately 6% decrease for a factor of 2 increase in Re). As a result, the comparison in Figure 8 is legitimate.

The source of the asymmetry of the mean product profiles for $\phi \neq 1$ can be seen in Figure 9. This figure is a plot in the spatial domain of the filtered product \tilde{Y}_P normalized by $Y_{P,st}$ for $\phi = 1/8, 1$ and 8 , at a time of $\tau = 19$. For $\phi = 1$, high values of product mainly occur in the cores of the large scale structures. For this case the product in the cores is somewhat uniformly distributed in agreement with experimental observations. This is seen more clearly in the central structure than for the outer ones. The outer structures have evolved from relatively recent pairing events while the central structure was formed earlier and has had more time for small scale mixing to break down mixture gradients in the core. The somewhat uniform distribution of product in the core regions results in the symmetric mean product profiles seen in Figure 7 and 8 for $\phi = 1$.

For $\phi = 1/8$ and 8 , however, Figure 9 shows the large

values of \tilde{Y}_P to shift toward the lower and upper sides of the layer respectively. This shift reflects the change in ξ_{st} for these cases given in Table 1. Although the flame shifts toward the lean side, the core regions still produce a large amount of product. Also note that the flame shifts to the left and right sides of the structures for $\phi = 1/8$ and 8 respectively. This behavior is indicative of streamwise gradients in the mixed fluid of the layer as will be discussed below.

The asymmetry of the mean profiles for $\phi \neq 1$ seen in Figure 7 results from the vertical shift of the flame toward the side lean in reactants, as expected from intuition. However, the degree of the asymmetry is moderated by the product formed due to the streamwise shift of the flame relative to the large scale structures. Product formed in the braid and core regions also moderate the asymmetry. These effects keep the shift in peak mean product from $\phi = 1/8$ to 8 to a relatively small value of $\simeq 25\%$ the width of the layer, even with the factor of 64 change in ϕ .

The streamwise shift of the flame observed in Figure 9 manifests itself as ramp structures in time trace plots of product or temperature commonly measured in experimental investigations. Ramp structures have been observed in the mixing layer experiments of M-D and Fiedler(1975) among others. Figure 10 is a trace plot through the spatial domain of the normalized product for $\phi = 1/8$ at $\tau = 19$. Traces for eight locations across the layer are shown in the figure. Each trace has been normalized by the maximum Y_P observed at all transverse locations. The vertical distance between the axes is therefore $Y_{P,max}$. The top of the figure is the $+x_2/\delta_{P_m}$ side of the layer and the bottom is the $-x_2/\delta_{P_m}$ side. The Y_P values in this figure are taken directly from the subgrid LEM fields and are not filtered. Two cycles of the spatial domain are shown in the figure and the horizontal axis is plotted as $-x_1$ to correspond with the experimental time traces of M-D. From the figure, large fluctuations in product are evident across the entire width of the layer in agreement with the observations of Brown and Roshko(1974). These fluctuations appear discontinuous due to the sampling technique used to generate the figure. The data plotted in Figure 10 only represents about 6% of the available subgrid data. As discussed earlier, these fluctuations are well resolved in the subgrid spatial domain. Streamwise ramp structures are also apparent across the layer. These ramps decrease from left to right in the figure but are hard to visualize owing to the large fluctuations.

The streamwise ramp structures in the layer are more evident in Figure 11. This is a similar trace plot but of the LES filtered product \tilde{Y}_P . Included in this figure are the traces for both $\phi = 1/8$ and 8. Also included are the time trace plots of M-D for the same values of ϕ . The data of M-D is the normalized temperature instead of the product. The simulated and experimental data may be compared, however, because, for the flow considered, the experimentally measured temperature is proportional to the product as described by M-D. The spatial filtering of the present

results removes many of the fluctuations seen in Figure 10 and smooths the trace plots. This smoothing effect has also removed many of the product fluctuations in Figure 9 as well. The experimental results have also been filtered locally as explained by M-D due to the low spatial resolution of the measuring probe. From Figure 11 note that the simulations have captured the ramp structures observed in the experiments. These structures have been highlighted with arrows in the predicted results for clarity (M-D shaded their ramp structures as seen in the figure). The simulations also capture the change in sign of the gradient of the ramps with a change from $\phi = 1/8$ to 8. The ramps in the simulations also appear more pronounced toward the center of the layer than at the edges as seen in the experiment.

Another subtle feature captured by the simulations can also be seen in Figure 11. In both the experimental and computational results, note that the product/temperature fluctuations are greater on the side of the layer lean in reactants than on the rich side. The lean side is on the top for $\phi = 8$ and the bottom for $\phi = 1/8$. This feature can also be seen in Figure 10. This behavior results for the skewness of ξ_{st} toward $\xi = 0$ or 1 for $\phi = 1/8$ or 8, respectively, as seen in Table 1. For example, with $\phi = 1/8$, a small change $\Delta\xi$ for $\xi < \xi_{st}$ results in a much larger change in product than for $\xi > \xi_{st}$. As a result, the fluctuations in ξ on the lean reactant side produce larger fluctuations in product/temperature.

M-D noted that the observed ramp structures result from streamwise gradients in the composition of mixed fluid in the layer. The mixed fluid can be quantified in terms of the mean mixed mixture fraction ξ_m defined by,

$$\xi_m = \frac{\int_{\epsilon}^{1-\epsilon} \xi \mathbf{p}^{sgs}(\xi) d\xi}{\int_{\epsilon}^{1-\epsilon} \mathbf{p}^{sgs}(\xi) d\xi} \quad (24)$$

where \mathbf{p}^{sgs} is the subgrid mixture fraction pdf. ξ_m is a measure of the mean value of the mixed fluid at a point. Figure 12 presents the predicted trace plots of ξ_m which correspond to the product traces in Figure 11. The figure shows that the streamwise gradients in ξ_m do appear in the simulations as ramp structures. These structures are decreasing in the figure from left to right. The sawtooth character of ξ_m on the top results from entrainment of pure fluid tongues into the layer. This also occurs on the lower side but is less evident since ξ_m are closer to zero.

Figure 12 also shows a transverse gradient in ξ_m across the layer in addition to the streamwise gradient. This is more clearly seen in Figure 13 which is a plot of the $\langle \xi_m \rangle_{mean}$. $\langle \xi_m \rangle_{mean}$ has been calculated as in equation (24) but using $\langle \mathbf{p}^{sgs} \rangle_{mean}$ instead of \mathbf{p}^{sgs} . Also included in the figure is the experimental data of Konrad(1976) and Koochesfahani and Dimotakis(1986) for mixing layers at comparable Reynolds numbers. This figure shows the present result to agree quite well with the experiments. Both the magnitude and gradient of $\langle \xi_m \rangle_{mean}$ are in good agreement over most of the layer. At the extremities, the present results deviate from the experimental data. Konrad's data does not extend to the extremities of the layer

and does not provide any guidance. The $\langle \xi_m \rangle_{mean}$ data from Koochesfahani and Dimotakis was calculated from the mean temperature data of M-D using an approximate technique (Koochesfahani and Dimotakis, 1986). The reliability of this technique at the extremities of the layer, where ξ_m is intermittent, is not known. As a result, additional experimental data is necessary to resolve the discrepancy at the layer edges between the predicted and experimental results.

M-D proposed an explanation for the development of the large scale gradients in ξ_m in terms of an idealized picture of vortex structure within mixing layers described by Bernal (1981). In this description, the primary large scale structures seen in Figure 9 are supplemented with small scale streamwise vortices embedded in the braid regions. These structures are commonly called "rib" vortices and partially wrap around the large scale primary structures. The rib vortices draw in and promote mixing of pure freestream fluid from the outside to the inside of the primary structures. This biases the local mixture toward the freestream fluid to which it is closest establishing the gradients in ξ_m .

The DNS simulations of Park *et al.* (1994) for pre-transitional mixing layers confirmed the importance of rib mixing in establishing the transverse gradient of $\langle \xi_m \rangle_{mean}$ seen in Figure 13. Park *et al.* also showed that purely 2-D simulations may produce a gradient in $\langle \xi_m \rangle_{mean}$ opposite to that shown in Figure 13 due to the lack of the 3-D small scale rib stirring. The LES-LEMC approach presented here, though only formulated in 2-D, models the effect of the 3-D rib stirring via the subgrid LEM stirring events and by the fluctuating velocity component included in the subgrid convection algorithm. This enables the LES-LEMC approach to capture the proper transverse gradients in $\langle \xi_m \rangle_{mean}$.

Figure 14 presents a spatial plot of the predicted subgrid ξ_m throughout the layer. An enlarged view of the central structure is also shown. As seen in the figure, there is a significant amount of mixing in the braid regions owing to the small scale stirring of the model. Small scale stirring around the edges of the primary structures is also seen to promote the transverse as well as streamwise large scale gradients in ξ_m . From the enlarged view of the central structure, an additional effect is apparent which also promotes the streamwise gradients. Most of the fluid from the lower side of the layer enters the primary structure from its lower left quadrant along the bottom side of the left-hand braid. The majority of fluid from the top stream conversely enters from the upper right-hand quadrant. A streamwise gradient in ξ across the structure is set up by this entrainment process. This gradient is then broken down by small scale stirring in the braids and by stirring in the outer streamwise extremities of the core. As a consequence, a streamwise gradient in ξ_m is generated. The combination of the small scale stirring around the edges of the primary structure and the streamwise entrainment of the bulk of freestream fluid result in an overall large scale gradient

in ξ_m which is aligned diagonally across the layer. This diagonal gradient contains the transverse and streamwise components observed in Figures 12 and 13.

This diagonally aligned gradient in ξ_m is made possible by the relatively small value of Schmidt number for gases. For liquids, Sc is of the order of 600 and molecular diffusion is therefore much less effective in mixing the freestream fluids. As a result, fluid entrained into the layer may circulate within the primary vortex core relatively unmixed for a significant amount of time. All the while small scale effects stir the fluid so that upon mixing ξ_m is almost uniform across the layer. This effectively eliminates both the streamwise and transverse gradients of ξ_m as has been observed in the liquid experiments of Koochesfahani and Dimotakis (1986). This emphasizes the importance of accurately capturing the effects of small scale stirring and diffusion even at high Reynolds numbers.

A parameter commonly measured in reacting mixing layer experiments is the product thickness δ_P defined by,

$$\delta_P = \int_{-\infty}^{+\infty} \frac{\langle [P] \rangle_{mean}}{[O]_o} dx_2 \quad (25)$$

where $[M]$ denotes is the concentration of species M . δ_P is a measure of the total product in the layer divided by the concentration of freestream reactants on the lower speed side. In the present simulation, the low speed side corresponds to lower side containing species O . Given the molecular weights and density specified in these simulations, equation (25) reduces to,

$$\delta_P = \int_{-\infty}^{+\infty} \frac{\langle Y_P \rangle_{mean}}{2Y_{O,o}} dx_2 \quad (26)$$

Figure 15 shows the variation of δ_P with equivalence ratio for the present simulations at a time of $\tau = 19$. In this figure δ_P has been nondimensionalized by δ_1 which is the length between the two points at which the mean product profile attains a value of 1% its peak mean value. Also included in this figure are predictions from the Broadwell-Breidenthal (B-B) model proposed by Broadwell and Breidenthal (1982) and modified by Broadwell and Mungal (1988).

The B-B model is an idealized description of reacting mixing layers in which product is produced from two sources. The first is homogeneously mixed lumps of fluid which correspond to the cores of the large scale coherent structures. The composition of these lumps is determined by mixing freestream fluid at the entrainment ratio. The second source of product is a flame sheet embedded in the braid region which separates unmixed fluid from the two sides of the layer. Following Broadwell and Mungal (1988) the normalized product thickness from the B-B model may be written as,

$$\frac{\delta_P}{\delta_1} = C_{Hom} P_{Hom} + C_{Flm} P_{Flm} \quad (27)$$

where P_{Hom} and P_{Flm} are the homogeneous and flame sheet contributions, respectively, and C_{Hom} and C_{Flm} are

calibration constants. Broadwell and Mungal(1988) give expressions for P_{Hom} and P_{Flm} for both infinite and finite rate chemistry. Given these expressions, the calibration constants must be determined from two independently specified conditions. The first of these conditions is to fix the value of δ_P/δ_1 in equation (27) equal to the predicted value from the present simulations at $\phi = 1/8$. The second condition is to specify the ratio of the flame sheet product to the total at $\phi = 1/8$. This ratio is denoted by the symbol f_B and is defined by,

$$f_B = \frac{C_{Flm}P_{Flm}}{C_{Hom}P_{Hom} + C_{Flm}P_{Flm}} \quad (28)$$

Given these two conditions, the results of the B-B model have been plotted in Figure 15 for $f_B = 0, .5$ and 1 along with the present data.

From Figure 15 note that the B-B model shows a corner at $\phi = 1$ for the case when there is no flame sheet contribution, i.e. $f_B = 0$. This corner results from burn out of the lean reactant in the homogeneous cores for ϕ less than the entrainment ratio, i.e. $\phi < 1$. This is discussed by M-D. From the figure, note that the present data is in good agreement with the B-B model for $f_B = .5$, except at $\phi = 1$ where the present data is lower. Figure 16 is a plot of the same data except δ_P/δ_1 has been multiplied by ξ_{st} and plotted as a function of ξ_{st} . This figure shows the symmetry of the present data about $\xi_{st} = 1$ indicating an entrainment ratio of one expected for the temporal simulations. This figure again shows that the present data compares well with the B-B model for $f_B = .5$. M-D also found their experimental data to agree closely with the B-B model for $f_B = .5$. Their data showed a large scatter around $\phi = 1$ with some data falling below that of the B-B model as observed in the present simulations.

The final topic investigated for the infinite rate chemistry cases is the variation of product formation with Reynolds number. This topic was investigated experimentally by Mungal *et al.*(1985) for the same hydrogen-fluorine chemistry used by M-D. Mungal *et al.*'s experiments showed that in the limit of fast chemistry the peak of the mean temperature/product profiles across the layer exhibits a decreasing trend with increasing Reynolds number. Mungal *et al.* also observed the product thickness to decay approximately linearly with the logarithm of Re. This behavior of the product thickness was investigated using the LES-LEMC approach assuming infinite rate chemistry. Re in the simulations was varied by changing the velocity difference U_o as did Mungal *et al.* Five cases were considered having $U_o = 71, 84, 100, 121$ and 148 m/sec. The viscosity was held constant for each run and equal to the value used in the previously described runs. ϕ for all cases was $1/8$ as in the experiments. N_{LEM} was taken as 400 except for the two cases of $U_o = 121$ and 148 m/sec which required $N_{LEM} = 600$ in order to properly resolve the subgrid. The initialization for each case was identical to the previously described runs except the velocity field(including the fluctuating component) was scaled to the proper value of U_o .

Figure 17 is a plot of the product thickness as a function of Reynolds number for these five cases. All data from these simulations was taken at a nondimensional time of $\tau = 19$. This corresponds to collecting data at a fixed downstream station in a spatial problem as in the experiments of Mungal *et al.*(1985). The product thickness in Figure 17 has been nondimensionalized by δ_2 which is the 1% thickness of the mean product profile normalized by the stoichiometric value listed in Table 1. The abscissa of this figure is in terms of the logarithm(base 10) of Re_2 where $Re_2 = U_o\delta_2/\nu$. Included in the figure is the experimental data of Mungal *et al.* The experimental data was originally nondimensionalized by the thickness δ_1 (defined below equation (26)) but has been rescaled in Figure 17 by δ_2 . This has been done because the thickness δ_2 is less sensitive to statistical errors than δ_1 for both the experimental and numerical data.

The experimental data in Figure 17 has been fit with a line of slope $-.05$ following Mungal *et al.*(1985). The figure shows the present simulations are in general good agreement with the experimental data. The present results slightly over predict the product thickness owing to the dependence of the mean product profile on the entrainment ratio, as discussed above. The predicted results also show an approximate linear decay of product thickness with Reynolds number as does the experimental data. A linear fit of the simulated data yields a slope of $-.0523$ in good agreement with the slope suggested by Mungal *et al.*

The slope of the product decay in Figure 17 has been used to determine the calibration coefficient C_τ in the LES-LEMC method. Recall from section 4 that C_τ determines the calibration of the subgrid stirring and diffusion processes in the LEM model. $C_\tau = 100$ has been used for all simulations. Varying C_τ was found to change the linear slope of the product decay. For $C_\tau > 100$ the slope became steeper than $-.0523$ and for $C_\tau < 100$ the slope became shallower. All tested values of C_τ produced an approximate linear decay of the product thickness. This lends some support to the notion that C_τ may be universal. C_τ could be adjusted to more closely match the slope of the present data to that of the experiments. Further refinements are futile, however, because of the limited amount and scatter of the experimental data. Additional experimental results are necessary in order to further refine the calibration of C_τ .

7.2 FINITE RATE CHEMICAL REACTION

Finite rate effects are included within the LES-LEMC approach through the production source terms in the subgrid diffusion equations. In the present context, the subgrid mixture fraction equation (7) is supplemented by the diffusion-production equation for the product species given in equation (8). The production rate in this equation is determined from equations (9)-(11) as described above. The rate parameter A_P is specified in terms of the Damköhler number which is defined as $Da = \tau_{conv}/\tau_{chem}$. τ_{conv} is a characteristic fluid-mechanical time scale taken here as the

time from the beginning of the simulation to the nondimensional time $\tau = 19$. The chemical time scale τ_{chem} is specified following Broadwell and Mungal(1988) as,

$$\tau_{chem} = \rho_o A_p Y_{F,o} / 2 \quad (29)$$

where ρ_o is the density of the inert diluent fluid. The factor of two in the denominator results from the fact that $W_P = 2W_F$.

Several simulations were conducted for various Damköhler numbers in the range $2.5 \leq Da \leq 80$. For these simulations, the fluid properties and the initialization for the velocity field, subgrid mixture fraction, etc. were the same as for the infinite rate case with $U_o = 71$ m/sec. In addition, the subgrid product mass fraction was initialized to zero. The equivalence ratio for these runs is specified as $\phi = 1/8$. Also, N_{LEM} was taken as 300 which was found to be adequate to properly resolve the subgrid fields, as described above.

Results for the normalized mean product across the layer at a time of $\tau = 19$ are shown in Figure 18 for $Da = 2.5, 5, 10$ and 40 . Also included in the figure is the result for the infinite rate case from Figure 7. Figure 18 shows that the area under the mean product curves decreases significantly with a decrease in Da . Also, note the progressive shift from the asymmetric profile at $Da = \infty$ to a more symmetric profile as Da is decreased. These two trends are in agreement with the observations of Mungal and Frieler(1988) who investigated Da effects in hydrogen-fluorine flames in turbulent mixing layers.

Figure 19 shows a streamwise trace plot of the filtered product in the layer at $\tau = 19$ for $Da = 2.5$. This plot was generated in the same manner as described previous for the other trace plots. \tilde{Y}_P in the figure has been normalized by the maximum unfiltered Y_P value obtained at any of the eight transverse measuring stations. This figure may be compared with the corresponding plot for infinite rate chemistry given in Figure 11a. In Figure 19, notice that the streamwise ramp structures seen for infinite rate chemistry have essentially disappeared. Also notice that the product in the finite rate case is much more uniformly distributed in the large scale structures. This is true in both the transverse and streamwise directions. As discussed above, the ramp structures in the infinite rate case result from streamwise gradients in ξ_m observed in Figure 12. ξ_m for both the finite and infinite rate cases is the same though no ramp structures are apparent for low Da . Mungal and Frieler(1988) also observed these trends in experimental trace plots at low Damköhler number.

Mungal and Frieler(1988) interpreted the features of their mean product and product trace measurements in terms of the idealized B-B model in the following way. Recall from the B-B model that product in a mixing layer is produced from homogeneously mixed regions(vortex cores) mixed at the entrainment ratio, and from strained flame sheets(braid regions) separating pure fluid from each side of the layer. For liquids with $Sc \gg 1$, the flame sheet contribution is negligible even for infinite rate chemistry due

to low molecular diffusivity and relatively short residence times in the braids. For gases with $Sc \simeq 1$, however, molecular mixing in the braid regions is much more significant. As a result, for infinite rate chemistry there is a significant amount of product formed in the braids as observed in Figure 9. For finite rate chemistry in gases with low Da , Mungal and Frieler(1988) suggest that much less product is formed in the braids due to low residence times. Given these considerations, Mungal and Frieler suggest that the symmetry in the mean product profile for gases at low Da and for liquids results from the homogeneously mixed core regions in the layer. They also suggest that the braid contribution for gases with high Da results in the asymmetric mean product profile observed in Figure 18.

This interpretation of product formation in mixing layers may be refined given the spatial product plots given in Figure 9c and Figure 20. Figure 20a is the filtered product normalized by $Y_{P,st}$ for the $Da = 2.5$ case with $\phi = 1/8$. By comparing Figure 9c and 20a, it is clear that there is much less product formed in the braid regions for the low Da case. This is true for the cores of the large scale coherent structures as well. Normalizing the product in Figure 20a by its maximum value(Figure 20b) shows more clearly where the peak values of product are formed. As discussed previously, the gradients in ξ_m across the large scale structures result in a shift of the peak product or flame to the lean reactant side of the layer as seen in Figure 9 for infinite rate chemistry. The flame in Figure 9 is aligned with the stoichiometric contour of ξ_m as expected for infinite Da . For $\phi \neq 1$, the asymmetry in $\langle Y_P \rangle_{mean}$ for this case is seen to result more from the flame shifting to the outer extremities of the large scale structures than from product formed in the braids. For low Da in Figure 20b, the flame shifts away from the $\xi_{m,st}$ contour and is distributed more evenly in the core regions as suggested by Mungal and Frieler(1988).

From Figures 9c and 20b it is clear that the tendency of $\langle Y_P \rangle_{mean}$ to become symmetric for low Da predominately results from a redistribution of the flame within the large scale structures, as opposed to a lack of product formation in the braid regions. This redistribution of the flame results from the combined effects of finite rate chemistry and gradients in mixed mean fluid across the layer. As discussed above, the large scale gradient in ξ_m is aligned diagonally across the layer. This effect cannot be captured in the idealized B-B model though the model makes good predictions compared with experimental results.

Finally, the effect of finite rate chemistry on the product thickness may be investigated in the present simulations. From Figure 18, the decrease in area under the $\langle Y_P \rangle_{mean}$ curves with a decrease in Da results in a reduction of total product in the layer as measured by the product thickness δ_P . Figure 21 presents a plot of the variation of product thickness with Da predicted by the LES-LEMC method for values of Da up to 80. Also included in this figure are the experimental results of Mungal and Frieler(1988) for mixing layers at two different values of U_o . The prediction

of the B-B model for an entrainment ratio of one has also been included. The B-B model result has been calibrated with $f_B = .5$ following Broadwell and Mungal(1988), and with the LES-LEMC predicted value at $Da = 80$. The figure shows good agreement of the present data with the experimental results over the entire range of Da . The B-B model also shows good agreement with both the present and experimental data.

In Figure 21 it is necessary to keep in mind the fact that the present simulations and the B-B model assume a constant reaction rate while the experimental reaction rate varied with temperature. Also, the experimental entrainment ratio was approximately 1.3 as opposed to 1 for the present temporal simulations. In spite of these differences, the agreement in Figure 21 is good. This result is not fortuitous, however, because results(not shown here) for a temperature like dependence of the reaction rate show similar good agreement. Also, changing the entrainment ratio from 1 to 1.3 in the B-B model only slightly changed the result.

8 CONCLUSIONS

The application of the LES-LEMC method has been described and implemented for the description of diffusion flame structure in turbulent reacting flows. This approach includes a more fundamental treatment of the effects of molecular diffusion, chemical reactions and small scale turbulent stirring than other LES closure techniques. This has been accomplished by way of the linear eddy mixing model. The LES-LEMC approach has been applied to mixing and reaction in turbulent mixing layers with negligible heat release. The analysis of the simulation results lead to the following conclusions:

1. The application of the LES-LEMC method to flows at realistic Reynolds numbers demonstrates the *tractability* of the approach even though a relatively large amount of subgrid information must be retained throughout the simulation. This has been accomplished without incorporating memory optimization schemes or taking advantage of parallel computer architecture. These additional aspects, however, may need to be incorporated for more challenging problems.
2. The 2-D implementation of the method considered in this study has demonstrated the ability to adequately model a physical flow in which 3-D effects are confined to only the small scales of motion. The small scale 3-D effects are modeled in the LES-LEMC approach via the subgrid stirring events and through the implementation of a fluctuating velocity component in the convection algorithm for the subgrid fluid elements.
3. The present approach has captured many of the qualitative trends observed in high Reynolds number turbulent reacting mixing layers. This approach has also

yielded good quantitative agreement for both infinite and finite rate chemistry for several important quantities that have been measured experimentally. Good agreement of the present approach compared with the idealized Broadwell-Breidenthal model has also been realized.

4. The results of the simulations have also yielded additional physical insight into the process of mixing and reaction in turbulent mixing layers. Namely, for gases in which the molecular diffusivity is relatively high, gradients in the mixed mean fluid occur in both the streamwise and transverse directions. The streamwise gradients are found to result mainly from the streamwise entrainment of unmixed fluid from each side of the layer. Small scale effects then mix the pure fluid as it enters the large scale coherent structures yielding the streamwise gradients. The simulation results also show that the combined effects of finite rate chemistry and the gradients in ξ_m result in a redistribution of the flame within the large scale structures when Da is reduced from fast to slow chemistry. This redistribution effect is found to have a dominating influence on the symmetry of the mean product/temperature profiles. This is in contrast to earlier speculation which attributed asymmetries in these profiles to production in the braid regions between the large scale structures.

ACKNOWLEDGMENT

This work was supported in part by the Office of Naval Research grants N00014-92-J-4030 and N00014-95-1-0163. Support for some of the computations was provided by the DOD High Performance Computing Center at WPAFB, Ohio and is gratefully acknowledged.

REFERENCES

- Bayliss, A., Parikh, P., Maestri, L., and Turkel, E. (1985). A Fourth-Order Scheme for the Unsteady Compressible Navier-Stokes Equations, ICASE Report No. 85-44.
- Bell, J.H. and Mehta, R.D. (1990). Development of a Two-Stream Mixing Layer from Tripped and Untripped Boundary Layers, *AIAA J.*, **28**, 12, pp. 2034-2042.
- Bernal, L.P. (1981). The coherent structure of turbulent mixing layers: I. Similarity of the primary vortex structure. II. Secondary streamwise vortex structure, Ph.D. Thesis, California Institute of Technology.
- Bilger, R.W. (1980). Turbulent Flows with Nonpremixed Reactants. In Libby, P.A. and Williams, F.A., editors, *Turbulent Reacting Flows*, pp. 65-113, Springer-Verlag, Berlin.
- Broadwell, J.E. and Breidenthal, R.E. (1982). A simple model of mixing and chemical reaction in a turbulent shear layer, *J. Fluid Mech.*, **125**, pp. 397-410.
- Broadwell, J.E. and Mungal, M.G. (1988). Molecular mixing and chemical reactions in turbulent shear layers, *Twenty-Second Symposium (International) on Combustion*, The Combustion Institute, pp. 579-587.

- Broadwell, J.E. and Mungal, M.G. (1991). Large-scale structures and molecular mixing, *Phys. Fluids A*, **3**, 5, pp. 1193-1206.
- Brown, G.L. and Roshko, A. (1974). On density effects and large structures in turbulent mixing layers, *J. Fluid Mech.*, **84**, 4, pp. 775-816.
- Calhoun, W.H. Jr., Menon, S., and Goldin, G.M. (1995). Comparison of Reduced and Full Chemical Mechanisms for NO_x Prediction in Nonpremixed Turbulent H_2 -Air Jet Flames, *Comb. Sci. Tech.*, **104**, pp. 115-141.
- Calhoun, W.H. Jr. and Menon, S. (1995). Unpublished data.
- Calhoun, W.H. Jr. (1996). Ph.D. Thesis, *in preparations*, Georgia Institute of Technology, Atlanta, Ga.
- Dimotakis, P.E. (1989). Turbulent Free Shear Layer Mixing, presented at the 27th Aerospace Sciences Meeting, Reno, Nevada, AIAA paper 89-0262.
- Erlebacher, G., Hussaini, M.Y., Speziale, C.G., and Zang, T.A. (1990). Toward the Large-Eddy Simulation of Compressible Turbulent Flows, ICSE Report No. 87-20.
- Fiedler, H.E. (1975). Transport of Heat Across a Plane Turbulent Mixing Layer, *Adv. Geophys.*, **18A**, pp. 93-109.
- Fornberg, B. (1977). A Numerical Study of 2-D Turbulence, *J. Comp. Phys.*, **25**, pp. 1-31.
- Frankel, S.H., Adumitroaie, V., Madnia, C.K. and Givi, P. (1993). Large Eddy Simulation of Turbulent Reacting Flows by Assumed pdf Methods. In Ragab, S.A. and Piomelli, U., editors, *Engineering Application of Large Eddy Simulations*, pp. 81-101, New York: ASME, FED-Vol. 162.
- Fureby, C. (1995). On Modeling of Unsteady Combustions utilizing Continuum Mechanical Mixture Theories and Large Eddy Simulations, Ph.D. Thesis, Lund Institute of Technology, Sweden.
- Fureby, C. and Möller, S.-I. (1995). Large Eddy Simulation of Reacting Flows Applied to Bluff Body Stabilized Flames, *AIAA J.*, **33**, 12, pp. 2339-2347.
- Gao, F., and O'Brien, E.E. (1993). A Large-Eddy Simulation Scheme for Turbulent Reacting Flows, *Phys. Fluids A*, **5**, pp. 1282-1284.
- Goldin, G.M. and Menon, S. (1996). A Linear Eddy Model for Steady-State Turbulent Combustion, presented at the AIAA 34th Aerospace Sciences Meeting, Reno, Nevada, AIAA paper 96-0519.
- Hariharan, N. and Sankar, L.N. (1994). Higher Order Numerical Simulation of Rotor Flow Field, AHS Forum and Technology Display, Washington, DC., May.
- Kee, R.J., Rupley, F.M. and Miller, J.A. (1989). Chemkin-II: A Fortran Chemical Kinetics Package for the Analysis of Gas Phase Chemical Kinetics, Sandia National Laboratories Report, SAND89-8009B.
- Kerstein, A.R. (1988). Linear-Eddy Model of Turbulent Scalar Transport and Mixing, *Comb. Sci. Tech.*, **60**, pp. 391-421.
- Kerstein, A.R. (1989). Linear-Eddy Model of Turbulent Transport II. Application to Shear Layer Mixing, *Comb. Flame*, **75**, pp. 397-413.
- Kerstein, A.R. (1990). Linear-Eddy Model of Turbulent Transport III. Mixing and Differential Molecular Diffusion in Round Jets, *J. Fluid Mech.*, **216**, pp. 411-435.
- Kerstein, A.R. (1991). Linear-Eddy Model of Turbulent Transport. Part 6: Microstructure of Diffusive Scalar Fields. *J. Fluid Mech.*, **231**, pp. 361-394.
- Kerstein, A.R. (1992). Linear-Eddy Model of Turbulent Transport 4. Structure of Diffusion-Flames, *Comb. Sci. Tech.*, **81**, pp.75-96.
- Kim, W.-W. and Menon, S. (1995). On the properties of a localized dynamic subgrid-scale model for large-eddy simulations, submitted to *J. Fluid Mech.*
- Koochesfahani, M.M., and Dimotakis, P.E. (1986). Mixing and Chemical Reactions in a Turbulent Liquid Mixing Layer, *J. Fluid Mech.*, **170**, pp. 83-112.
- Konrad, J.H. (1976). An experimental investigation of mixing in two-dimensional turbulent shear flows with application to diffusion-limited chemical reactions, Ph.D. Thesis, California Institute of Technology.
- Liou, M.-S., and Steffen, C.J. (1993). A New Flux Splitting Scheme, *J. Comp. Phys.*, **107**, pp. 23-39.
- Magnussen, B.F., and Hjertager, B.H. (1976). On Mathematical Modeling of Turbulent Combustion with Special Emphasis on Soot Formation and Combustion, *Sixteenth Symposium (Int.) on Combustion*, The Combustion Institute, pp. 719-729.
- McMurthy, P.A., Riley, J.J., and Metcalfe, R.W. (1989). Effects of Heat Release on the Large-scale Structure in Turbulent Mixing Layers, *J. Fluid Mech.*, **199**, pp. 297-332.
- McMurtry, P.A., Menon, S., and Kerstein, A.R. (1992). A Subgrid Mixing Model for Nonpremixed Turbulent Combustion, presented at the AIAA 30th Aerospace Sciences Meeting, Reno, Nevada, AIAA paper 92-0234.
- McMurtry, P.A., Gansauge, T.C., Kerstein, A.R. and Krueger, S.K. (1993). Linear eddy simulations of mixing in a homogeneous turbulent flow, *Phys. Fluids A*, **5**, 4, pp. 1023-1034.
- McWilliams, J.C. (1984). The emergence of isolated coherent vortices in turbulent flow, *J. Fluid Mech.*, **146**, pp. 21-43.
- Menon, S. (1991). Active Control of Combustion Instability in a Ramjet Using Large-Eddy Simulations, presented at the AIAA 29th Aerospace Sciences Meeting, Reno, Nevada, AIAA paper 91-0411.
- Menon, S., and Jou, W.H. (1991). Large-Eddy Simulations of Combustion Instability in an Axisymmetric Ramjet Combustor, *Comb. Sci. Tech.*, **75**, pp. 53-72.
- Menon, S., and Kerstein, A.R. (1992). Stochastic Simulation of the Structure and Propagation Rate of Turbulent Premixed Flames, *Twenty-fourth Symposium (Int.) on Combustion*, The Combustion Institute, pp. 443-450.
- Menon, S., McMurtry, P.A., and Kerstein, A.R. (1993a). A Linear Eddy Subgrid Model for Turbulent Combustion: Application to Premixed Combustion, presented at the AIAA 31st Aerospace Sciences Meeting, Reno, Nevada, AIAA paper 93-0107.
- Menon, S., McMurtry, P.A., and Kerstein, A.R. (1993b). A Linear Eddy Subgrid Model for Turbulent Combustion: Application to Premixed Combustion. In Galperin, B. and Orszag, S.A., editors, *Large Eddy Simulation of Complex Engineering and Geophysical Flows*, pp. 287-314, Cambridge University Press, Cambridge.
- Menon, S., McMurtry, P.A., Kerstein, A.R. and Chen, J.-Y. (1994). A New Mixing Model to Predict NO_x Production in a Turbulent Hydrogen-Air Jet Flame, *J. Propulsion Power*, **10**, 2, pp. 161-168.
- Michalke, A. (1964). On the inviscid instability of the hyperbolic-tangent velocity profile, *J. Fluid Mech.*, **19**, 4, pp. 543-556.

Moin, K, Squires, W., Cabot, W. and Lee, S. (1991). A dynamic subgrid-scale model for compressible turbulence and scalar transport, *Phys. Fluids A*, **3**, 11, pp.2746-2757.

Mungal, M.G., and Dimotakis, P.E. (1984). Mixing and Combustion with Low Heat Release in a Turbulent Shear Layer, *J. Fluid Mech.*, **148**, pp. 349-382.

Mungal, M.G., Hermanson, J.C. and Dimotakis, P.E. (1985). Reynolds Number Effects on Mixing and Combustion in a Reacting Shear Layer, *AIAA J.*, **23**, 9, pp. 1418-1423.

Mungal, M.G. and Frieler, C.E. (1988). The Effects of Damköhler Number in a Turbulent Shear Layer, *Comb. Flame*, **71**, pp.23-34.

Nelson, C.C. (1995). Private communication.

Park, K.-H., Metcalfe, R.W. and Hussain, F. (1994). Role of coherent structures in an isothermally reacting mixing layer, *Phys. Fluids A*, **6**, 2, pp. 885-902.

Pope, S.B. (1979). The statistical theory of turbulent flames, *Phil. Trans. Royal Soc. London*, **291**, pp. 529-568.

Pope, S.B. (1990). PDF methods for turbulent combustion: progress and challenges, *Twenty-third Symposium (Int.) on Combustion*, The Combustion Institute, pp. 591-612.

Ramshaw, J.D., O'Rourke, P.J. and Stein, L.R. (1985). Pressure Gradient Scaling Method for Fluid Flow with Nearly Uniform Pressure, *J. Comp. Phys.*, **58**, pp. 361-376.

Riley, J.J., and Metcalfe, R.W. (1980). Direct Numerical Simulations of a Perturbed, Turbulent Mixing Layers, presented at the AIAA 18th Aerospace Sciences Meeting, Pasadena, California, AIAA paper 80-0274.

Roshko, A. (1976). Structure of Turbulent Shear Flows: A New Look, *AIAA J.*, **14**, 10, pp. 1349-1357.

Schumann, U. (1989). Large-eddy simulation of turbulent diffusion with chemical reactions in the convective boundary layer, *Atmos. Env.*, **23**, 8, pp. 1713-1727.

Sykes, R.I., Henn, D.S., and Parker, S.F. (1992). Large-Eddy Simulation of a Turbulent Reacting Plume, *Atmos. Env.*, **26A**, 14, pp. 2565-2574.

Smith, T.M., Menon, S., and McMurtry, P.A. (1994). The Structure of Premixed Flames in Isotropic and Shear Driven Turbulent Flows, presented at the 32nd Aerospace Sciences Meeting, Reno, Nevada, AIAA paper 94-0677.

Tennekes, H. and Lumley, J.L. (1972). *A First Course in Turbulence*, MIT Press, Cambridge, MA.

Williams, F.A. (1985). *Combustion Theory*, 2nd ed., The Benjamin/Cummings Publishing Company, Menlo Park, CA.

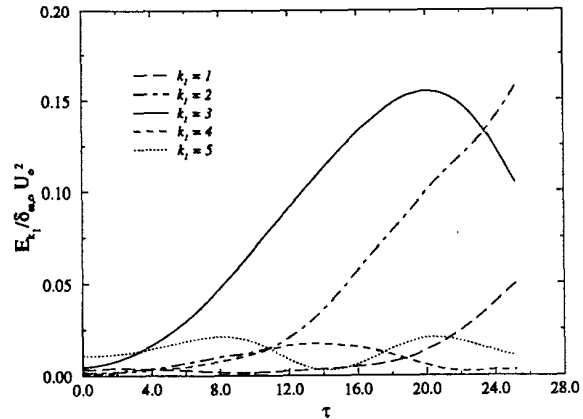


Figure 1. Temporal evolution of the streamwise modal energies of the mixing layer.

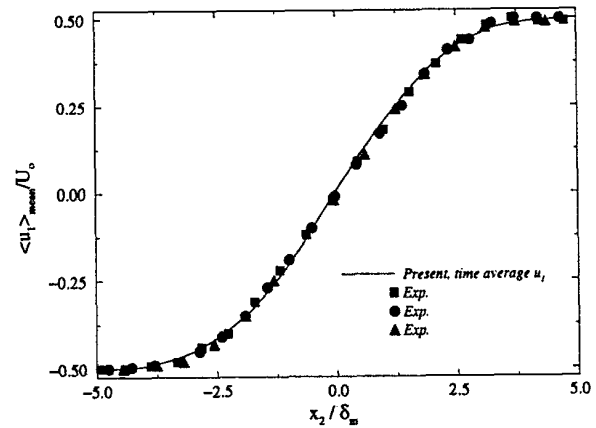


Figure 2. Mean streamwise velocity profile plotted in a similarity coordinate. Experimental data from Bell and Mehta(1990) for a tripped layer measured at three different streamwise stations.

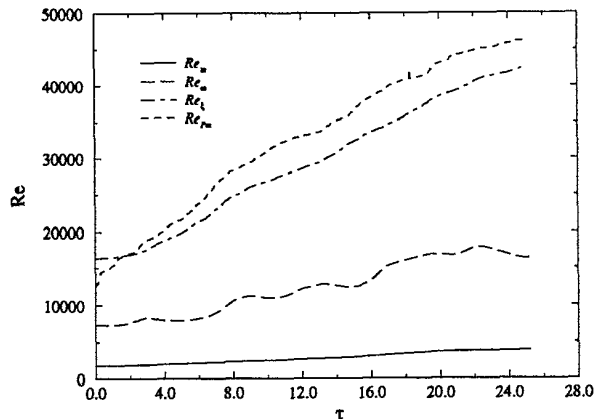


Figure 3. Temporal evolution of Reynolds number based on various transverse length scales. This plot is equivalent to a plot of the various normalized length scales themselves.

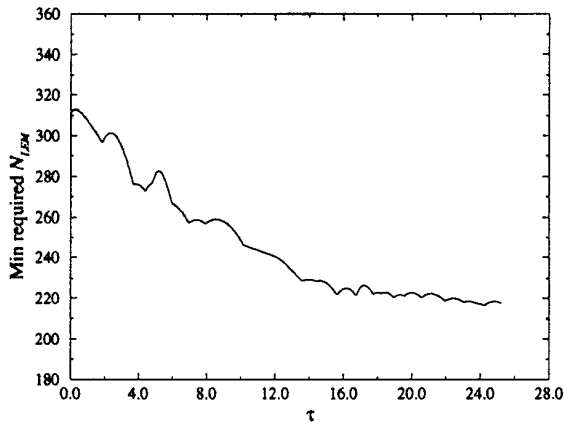


Figure 4. Temporal evolution of the minimum required subgrid LEM resolution in the simulation domain.

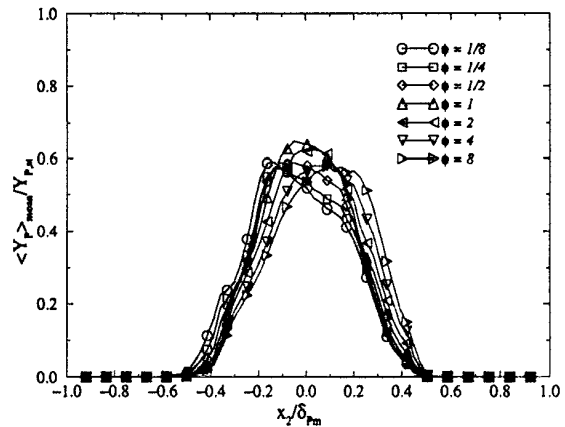


Figure 7. Mean product mass fraction normalized by stoichiometric product(see Table 1), $\tau = 19$.

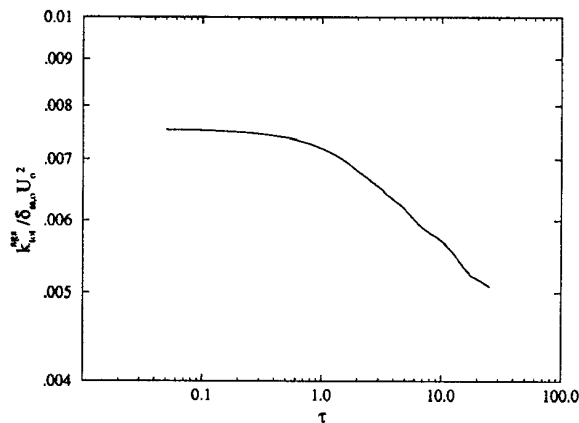


Figure 5. Temporal decay of the integrated mean subgrid kinetic energy, k_{tot}^{sgs} .

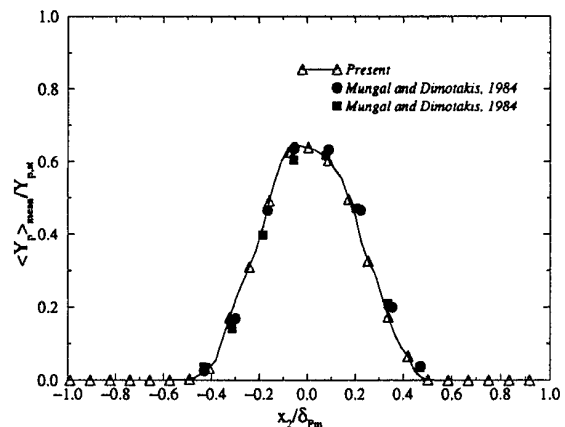


Figure 8. Comparison of predicted normalized mean mass fraction at $\tau = 19$ for $\phi = 1$ with two sets of experimental data from Mungal and Dimotakis(1984).

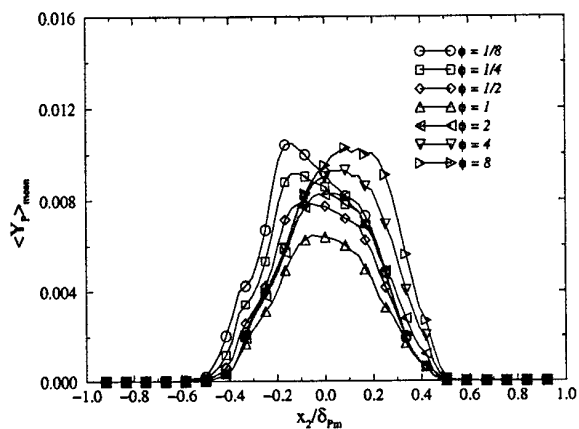


Figure 6. Mean product mass fraction across the layer for various values of equivalence ratio, $\tau = 19$.

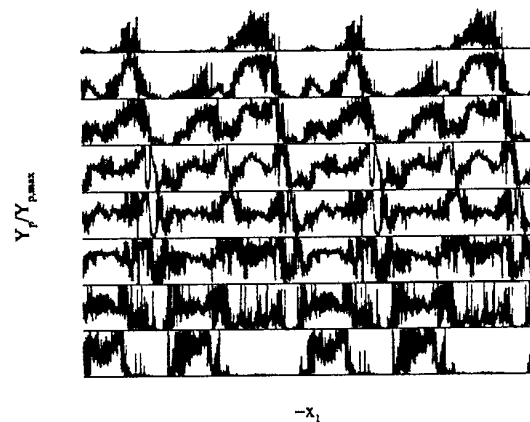


Figure 10. Streamwise trace plots of subgrid product mass fraction, $\phi = 1/8$. Measuring stations from bottom to top are : $x_2/\delta_{Pm} = -0.33, -0.25, -0.14, -0.05, +0.06, +0.17, +0.25, +0.36$. Two cycles of the spatial domain are plotted.

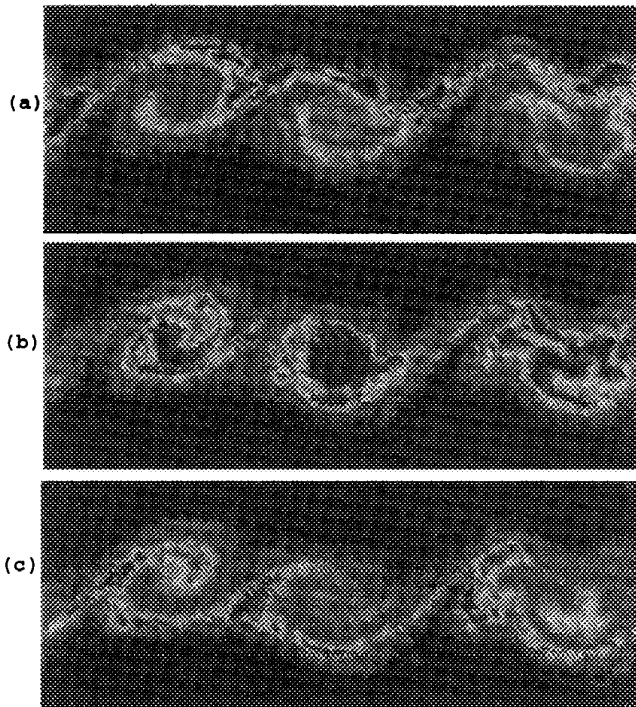



Figure 9. Spatial plot of the filtered product mass fraction at $\tau = 19$; (a) $\phi = 8$, (b) $\phi = 1$, (c) $\phi = 1/8$. The top of each plot corresponds to x_2/δ_{Pm} positive. Legend: 0.  .95.

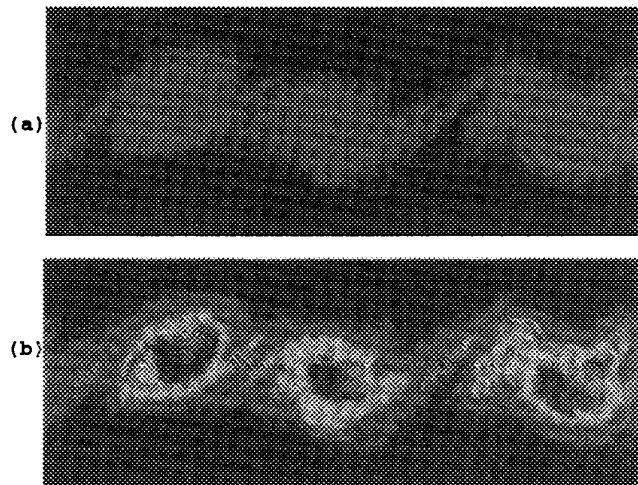




Figure 20. Spatial plot of the filtered product mass fraction at $\tau = 19$ for $\phi = 1/8$ and $Da = 2.5$; (a) normalized by stoichiometric value as in Figure 9, (b) normalized by the maximum value. Legend: (a) 0.  .95, (b) 0.  1.

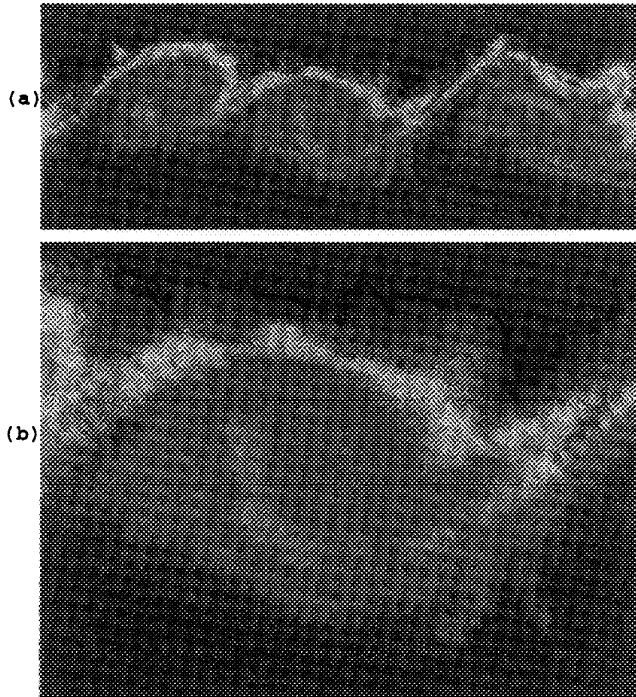



Figure 14. Spatial plot of the subgrid mixed mean mixture fraction at $\tau = 19$; (a) entire streamwise width of the domain, (b) enlarged view of the central structure. Legend: 0.  1.

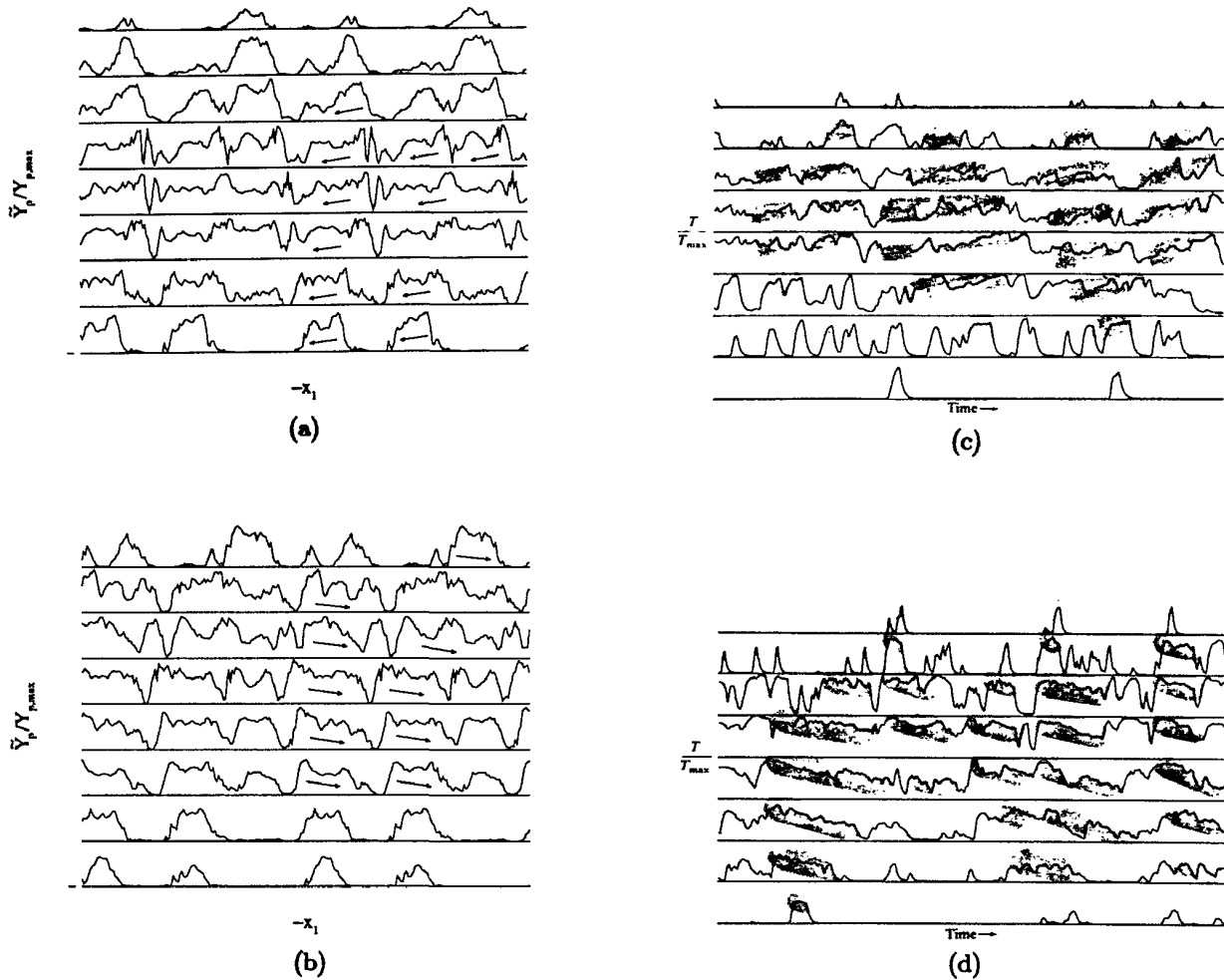


Figure 11. Trace plot of product in the layer. (a) and (b) are predicted filtered product for $\phi = 1/8$ and 8 , respectively, measured at the same stations as in Figure 10. (c) and (d) are experimental temperature traces from Mungal and Dimotakis(1984) for $\phi = 1/8$ and 8 , respectively, measured at $x_2/\delta_{pm} = -.44, -.31, -.18, -.06, +.08, +.20, +.33, +.46$.

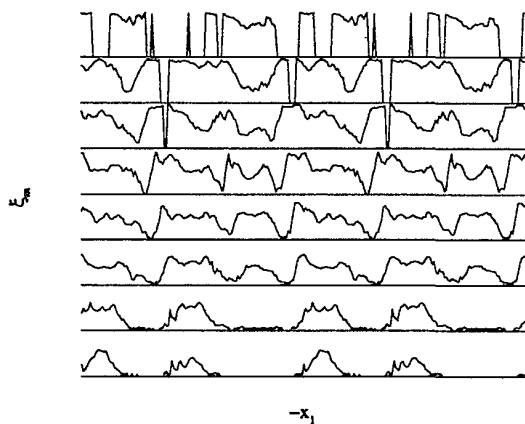


Figure 12. Predicted subgrid mixed mean mixture fraction traces; measuring stations the same as in Figure 10.

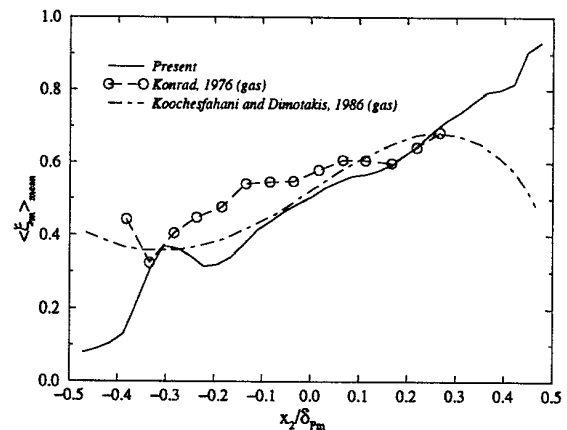


Figure 13. Mean mixed mean mixture fraction across the layer. Predicted result at $\tau = 19$; experimental data for gases from Konrad(1976) and Koochesfahani and Dimotakis(1986).

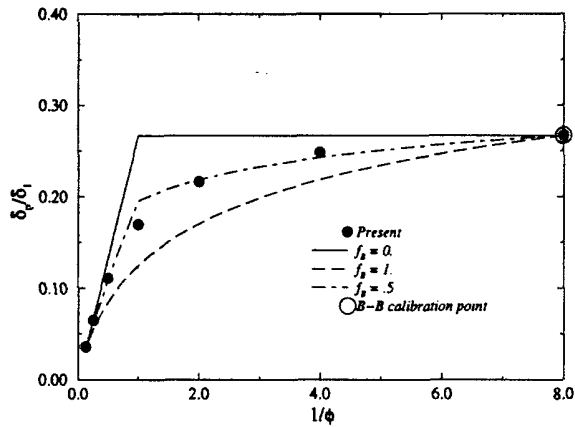


Figure 15. Dependence of product thickness with the inverse of equivalence ratio; present data compared with B-B model for three values of f_B . The large open circle denotes the calibration point of the B-B model.

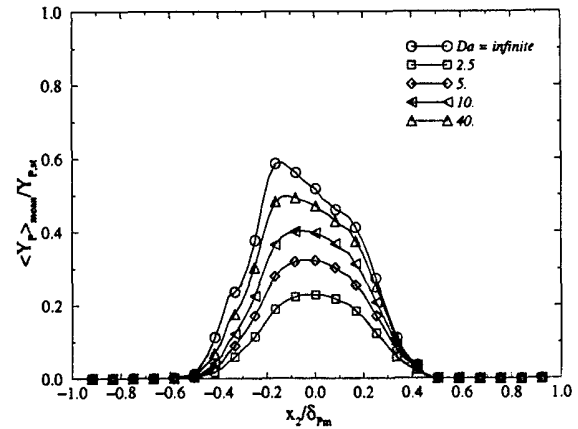


Figure 18. Mean normalized product across the layer at $\tau = 19$ for various values of Damköhler number.

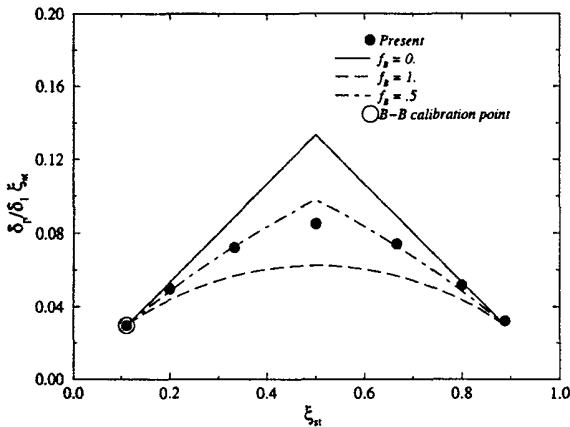


Figure 16. Variation of normalized product thickness with mixture fraction; present data compared with B-B model for three values of f_B . The large open circle denotes the calibration point of the B-B model.

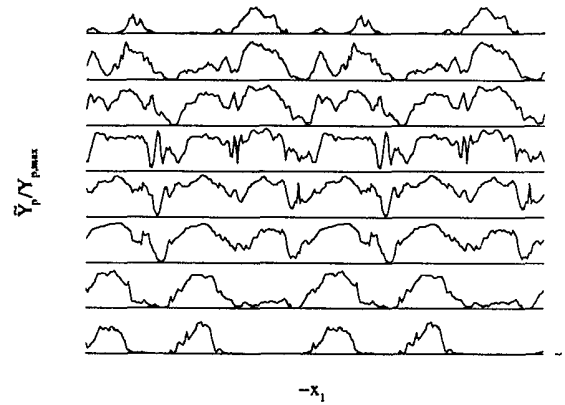


Figure 19. Trace plot of predicted filtered product in the layer for $\phi = 1/8$ and $Da = 2.5$ at $\tau = 19$; measured at the same stations as in Figure 10.

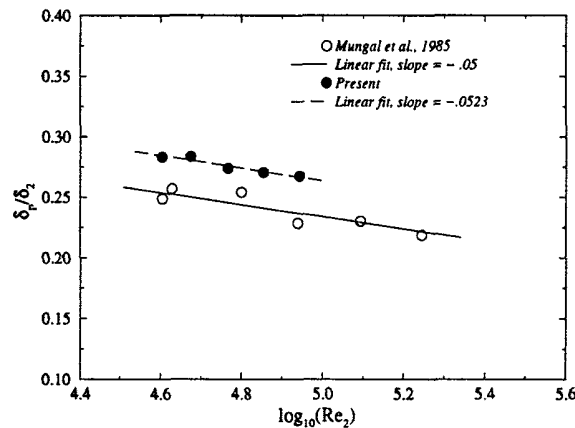


Figure 17. Product thickness dependence on Reynolds number; present data at $\tau = 19$ compared with experiments of Mungal *et al.*(1985).

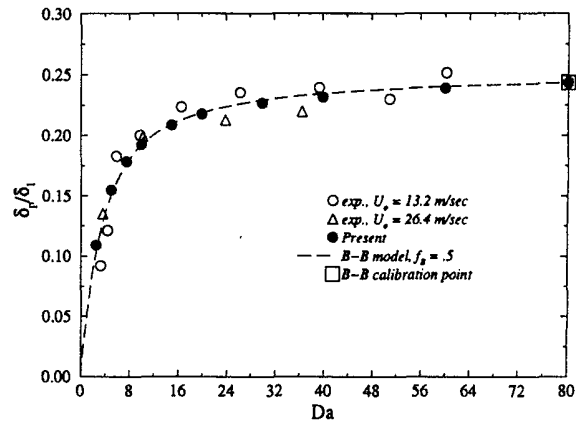
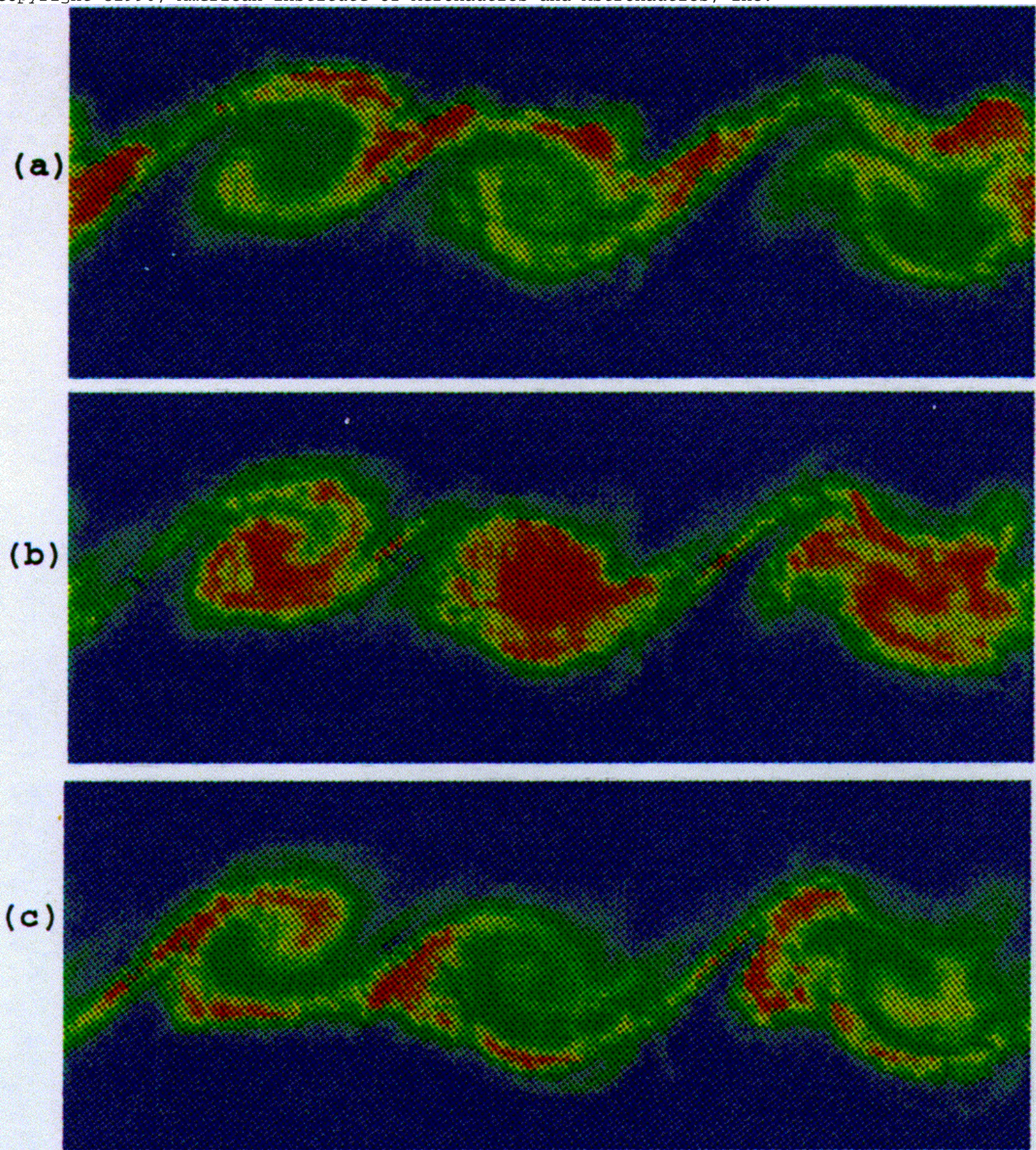
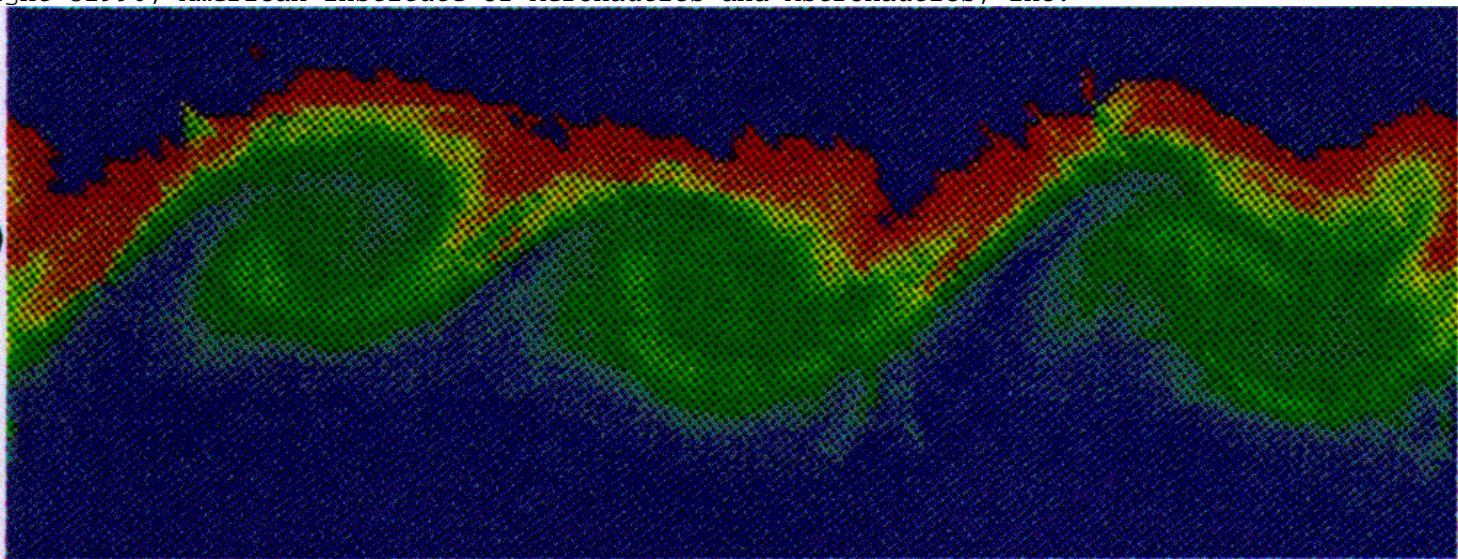


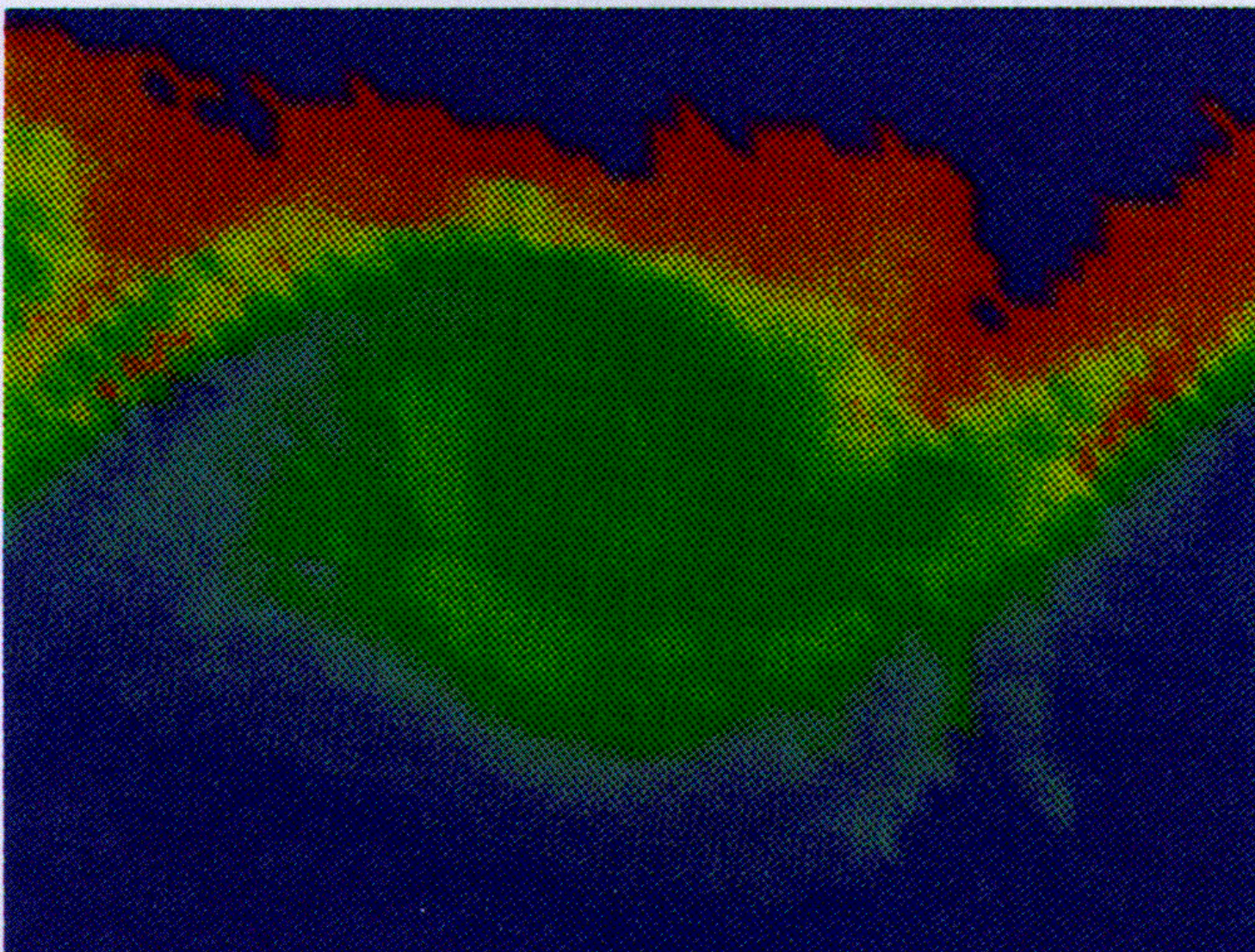
Figure 21. Dependence of product thickness on Damköhler number. Present data at $\tau = 19$; experimental data from Mungal and Frieler(1988) for two values of U_o ; B-B model for $f_B = .5$, large open square denotes the calibration point.



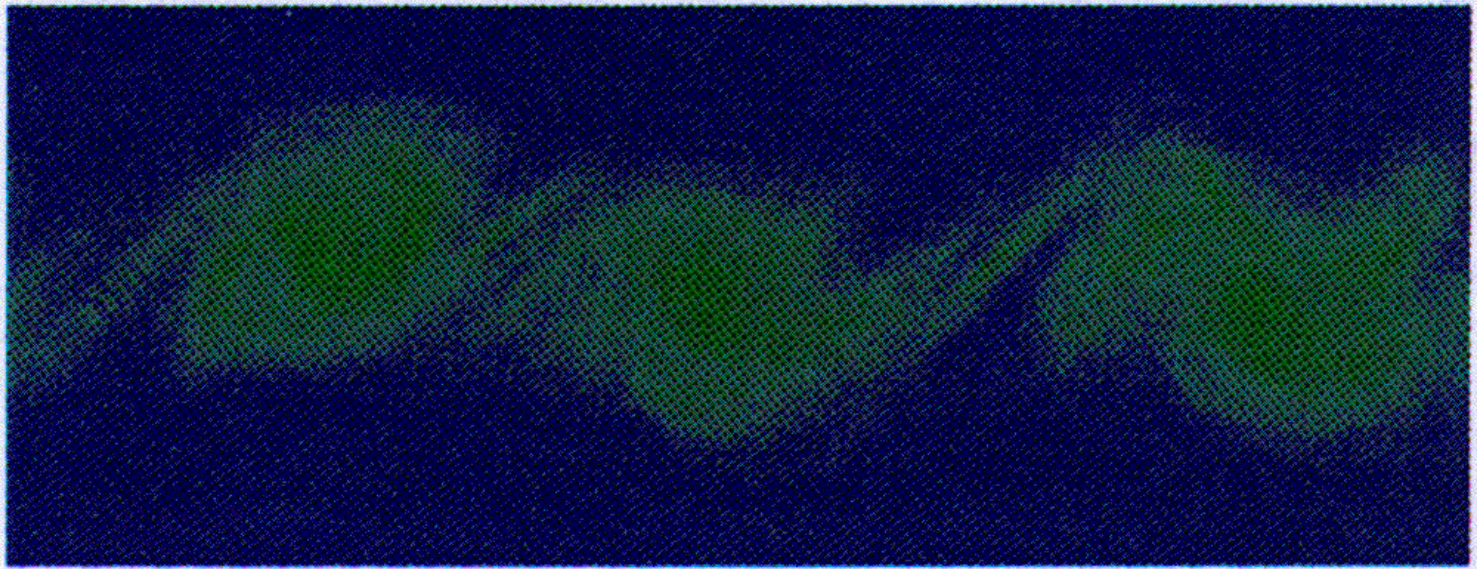
(a)



(b)



(a)



(b)

